Romanian Reports in Physics, Vol. 68, Supplement, P. S799–S845, 2016

GAMMA-BEAM INDUSTRIAL APPLICATIONS AT ELI-NP

G. SULIMAN[1], V. IANCU[1,*], C.A. UR[1], M. IOVEA[2], I. DAITO[3], H. OHGAKI[3]

[1]ELI-NP, "Horia Hulubei" National Institute for Physics and Nuclear Engineering, 30 Reactorului Street, RO-077125, Bucharest-Magurele, Romania
[2]Accept Pro 2000, Nerva Traian 1, K6, Apt 26, Bucharest, RO-031041, Romania
[3]Institute of Advanced Energy, Kyoto University, Uji, Kyoto 6110011, Japan
[*]Corresponding author *E-mail*: violeta.iancu@eli-np.ro

Abstract. An ultra-bright, energy tunable and monochromatic gamma-ray source in the range of 0.2–19.5 MeV produced by Laser-Compton Backscattering technique is ideal for non-destructive testing applications. Consequently, this source satisfies the criteria for large-size product investigations with added capabilities like isotope detection through the use of nuclear resonance fluorescence (NRF) technique. This document presents the technical description of two major industrial applications of gamma beams envisaged at ELI-NP: industrial applications based on NRF and industrial radioscopy and tomography. Both applications exploit the unique characteristics of the gamma beam to deliver new opportunities for the industry. The non-destructive assay based on high-brightness gamma rays can be successfully applied for safeguard applications and management of radioactive wastes. Radioscopy and computed tomography performed at ELI-NP has the potential to achieve high spatial resolution and high contrast sensitivity. The performance of the experimental setups proposed is discussed in detail in sections 2.3 and 3.3; the performance figures cited there are based on analytical calculations and numerical simulations.

Key words: Nuclear resonance fluorescence, radiography and computed tomography, high-intensity gamma beams.

1. INTRODUCTION

The White Book of the Extreme Light Infrastructure-Nuclear Physics (ELI-NP) project [1] proposes a series of applications that take advantage of the outstanding quality of the gamma beam available at ELI-NP. From the possible applications mentioned in the White Book, this Technical Design Report (TDR) describes the potential experiments that use the brilliant gamma beam for non-destructive investigations, such as industrial gamma beam tomography and nuclear resonance fluorescence (NRF) based applications.

An ultra-bright, energy-tunable and monochromatic gamma-ray source in the range of 0.2–19.5 MeV produced by Laser-Compton Scattering (LCS) technique is ideal for the non-destructive testing (NDT) applications. Practically, using this source is possible to detect and/or measure nuclides in an object non-destructively, which is a key technology for nuclear industrial applications such as management of radioac-

tive wastes, nuclear material accounting and safeguards. Moreover, the new source could be a perfect solution for fulfilling all technical requirements for the large-size and complex product investigations in aeronautics, automotive, die-cast or sintered industries, new materials and technologies development, for archaeological artifacts and work of art objects analysis and many others [1].

The design of the experiments and the estimation of the achievable counting rates and measurement times are highly dependent on the assumed parameters of the beam delivered by the machine. As a starting point for the estimates in this TDR we have used the values detailed in the Technical Design Report published by the EuroGammaS collaboration in Ref. [2].

Another version of the parameters of the source is shown on the webpage of the ELI-NP project: http://www.eli-np.ro/documents/ELI-NP-GBS-Specifications-rev3-1.pdf. These two documents are in total agreement and the comparison between the values significant for the present TDR is explained in the following.

Time-average spectral density at the peak energy *versus* spectral density [1/(s·eV)]. The range of (0.8–4.0)$\times 10^4$ photons/s·eV is the same in both tables, with the added benefit that the table in Ref. [2] details the inverse correlation between the energy of the photon beam and the achievable spectral density. This spectral value is used in the present TDR for estimating the number of NRF photons being detected by the ELI-NP Array of Detectors (ELIADE) array. Table 8 uses for the number of incoming photons the value of 50000 ph/s Γ_D calculated using 28000 ph/s·eV, representing a conservative estimate of the spectral density at 2.1 MeV, (the resonance energy of the uranium line) and 1.78 eV for the width of the resonance.

Number of photons/s within the bandwidth. The number of photons/s coming from the source is not present in the table linked from the web page of the project, but it is shown in the TDR of the gamma source [2]. This value can be estimated using the value of the spectral density, the energy of the beam and the bandwidth. For example, for a beam of 2 MeV, bandwidth of 0.5% and spectral density of 4×10^4 ph/s·eV an estimate of the total number of photons can be obtained as:

$$\begin{aligned} Photons/s = SpectralDensity \times energy \times bandwidth = \\ 4 \times 10^4 \times 5 \times 10^{-3} \times 2 \times 10^6 = 4 \times 10^8 photons/s, \end{aligned} \tag{1}$$

which is in agreement with the value shown in Ref. [2]. It should be noted that while the spectral density is decreasing by a factor or 5 over the whole energy range, the total number of photons/s within the bandwidth increases slightly. These values are used in the present TDR for estimating the background in NRF experiments and also in estimating the measurement time needed in the tomography setup. In some cases we have used a conservative value of 10^8 photons/s, or where it was the case, a value of 10^6 photons/macrobunch, derived from this value.

2. INDUSTRIAL APPLICATIONS BASED ON NRF

2.1. INTRODUCTION

The nuclear resonance fluorescence (NRF) is an attractive non-destructive analysis method because it provides signatures for a wide variety of materials, signatures that can be used to characterize the irradiated samples. Its use for detecting special nuclear materials within cargo containers was proposed by Bertozzi *et al.* [3] and subsequently developed by several organizations like Passport Systems, Inc., Pacific Northwest National Laboratory (PNNL) and Lawrence Livermore National Laboratory (LLNL) which have explored various research issues related to applications based on NRF [5–8]. The Department of Energy, USA, commissioned a report [4], which investigated the possible applications of NRF and the associated research challenges. The topics identified are mostly related to special nuclear materials (SNM) and nuclear safeguards applications such as U enrichment confirmation of UF_6 canisters, geo-sourcing of material, weapons dismantlement verification, direct measurement of Pu in spent fuel, analysis of gas samples, characterization of suspect material, and verification of SNM in a cargo container [4]. These topics were extensively studied in recent years using mostly continuous Bremsstrahlung sources and only few LCS sources [5–14].

Apart from SNM and nuclear safeguards applications, NRF-based applications for chemical compounds and organic materials have been proposed and demonstrated recently. Hayakawa *et al.* [12] demonstrated the non-destructive inspection of a shielded explosive by using NRF measurement, and succeeded to extract the abundance ratio of chemical components, $^{12}C/^{14}N$, of melamine compound. Beck *et al.* [15] used NRF to determine the ^{13}C content in diamond in concentrations as small as 0.5 mg, confirming the results of Raman scattering while demonstrating the feasibility of identifying mg quantities in a target. In the future, non-destructive measurements of heavy element contaminates in foods can also be envisaged. The maximum concentrations of the heavy metal contaminates in food established by Codex [16] are in the range of 0.1 mg/kg up to 200 mg/kg, well within the range of NRF methods.

As noted above, the applicability of the NRF method is quite general and broad. Moreover, the NRF method can be used in conjunction with tomography to produce elemental maps in objects of various compositions [17–20]. Lakshmanan *et al.* in a Monte Carlo simulations study proposed to use NRF imaging for visualizing breast cancer lesions [17]. Recently a 2D-image of isotope distribution of ^{208}Pb was demonstrated by using NRF by Toyokawa *et al.* [18]. In contrast to other nuclear methods used for composition analysis (activation analysis, elastic recoil analysis, accelerator mass spectroscopy) NRF requires very limited manipulation of the materials and does not noticeably affect the investigated objects. This, in turn, extends the potential uses of NRF methods to characterizing the internal structure of valuable objects like

historical artifacts, archeological objects, and works of art.

The two detection schemes used for NRF-based investigations are the scattering and the transmission method. In both cases interrogating photons are used to induce the resonant absorption while the de-excitation photons are detected either in a backscattering geometry or in a self-absorption (transmission) geometry [21]. The applications described here take in consideration both measuring schemes. As a result, the present TDR will propose two experimental setups at ELI-NP, one for each of the measurements schemes. The detailed description and rate estimates for the many of the possible applications are challenging due to the lack of information concerning the cross section and level widths of the nuclei of interest. As a result, measurements aimed at improving the quality of the NRF measurements for applications will also be a part of the experimental efforts proposed to be carried out at ELI-NP.

2.2. METHODS

2.2.1. Scattering NRF measurements

The general setup employed in the scattering NRF experiments is illustrated in Fig. 1. Here the investigated object is placed in the beam and the resonant photons are detected in a backscattered geometry by a detector located off-beam. Except the resonant photons, all other scattered photons have low energy due to the nature of Compton scattering. Therefore the high-energy resonant photons should be easily distinguished.

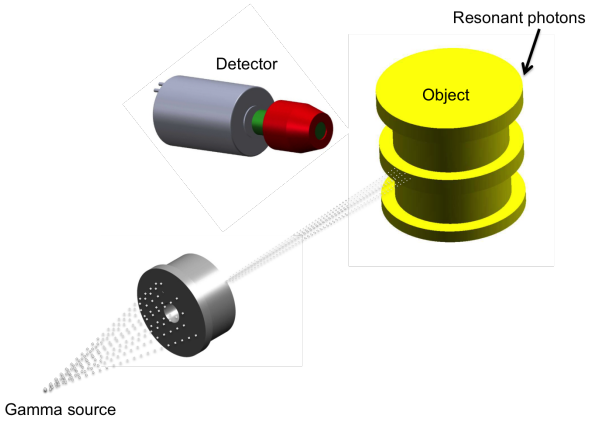

Fig. 1 – Schematic view of the backscattering NRF setup.

Hagmann *et al.* [5] performed Monte Carlo simulations for such geometry at a γ-ray flux of 10^{13} /s, which corresponds to a spectral density of flux of 10^{10} /s/keV.

They concluded that using NRF with these source parameters would allow detection of low concentration of U-238, 1 Bq/g, in a practical measurement time of 100 s [5]. The future gamma source from ELI-NP is expected to be a few orders of magnitude lower in intensity, which would mean that measuring higher concentrations could be achieved in still practical experimental times of a few hours.

2.2.2. Transmission NRF measurements using the notch method

The second detection method proposed for NRF measurements is the self-absorption or the transmission method (see Fig. 2) [21]. In this method the object-transmitted gamma beam strikes a sample (witness foil) that contains an isotope of interest. Same isotope is expected to exist in the investigated object in smaller concentrations. The detection of resonant photons scattered by the witness foil is done with a off-beam detector in a backscattering geometry, often referred to as the "notch detector". The flux of the transmitted off-resonance photons may be detected using a detector placed downstream of the witness foil in the beam as pictured in Fig. 2. Collimators may be used to define the beam and to remove scattered radiation. Contrary to the scattering NRF detection method where the photons that undergo NRF in the object are registered in the detector, in the transmission method the notch detector measures the attenuation of the resonant photons in the witness foil. A preferential attenuation of the resonant photons in the witness foil would indicate the presence of that isotope of interest in the investigated object [9, 21].

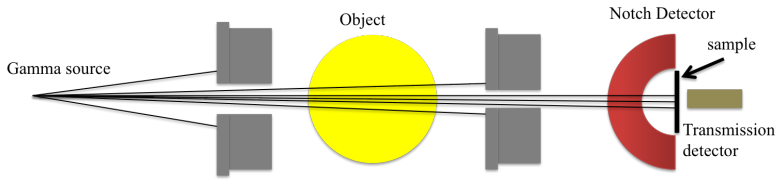

Fig. 2 – Schematic view of the transmission NRF setup.

The applicability of the transmission method is limited by the thickness of the investigated objects. Ludewigt *et al.* [9] give an overview of the use of NRF methods for three potential safeguard applications: "the isotopic assay of spend nuclear fuel, the measurement of ^{235}U enrichment in UF_6 cylinders and the determination of ^{239}Pu in mixed oxide (MOX) fuel". The main challenge encountered in these applications is obtaining enough statistics to ensure low uncertainties. As an alternative to bremsstrahlung beam, intense quasi-mononenergetic beams with small energy spread may be the solution to overcome this challenge. Shorter measurement times could potentially be achieved with intense quasi-monoenergetic photon sources like those delivered by ELI-NP. Estimation of the expected counting rate by use of transmission

method will be described in section 2.3.3.

2.2.3. Level widths and cross sections in support of NRF applications

The gamma beam at ELI-NP, together with the proposed array of detectors are the perfect tool for measuring the level widths and the NRF cross sections of nuclei of interest for applications. The lack of reliable data on the resonances of many of the stable or long-lived nuclei precludes the development of a sustained measurement program. For example, in the case of spent nuclear fuel (SNF) it is still unknown if ^{240}Pu has sufficiently strong resonances to make measurements possible [9]. The situation is the same for most of the other transuranic isotopes. The situation is usually not better for lighter nuclei that could be of interest for the applications outlined in the previous sections. As a result dedicated measurements to accurately determine the resonance cross sections will be performed for most of the isotopes of interest.

2.3. FEASIBILITY OF THE PROPOSED METHODS IN ELI-NP CONTEXT

2.3.1. Numerical simulations

One of the main advantages of using the gamma beam at ELI-NP for applications based on NRF is the availability of an advanced detector array, which can enhance by an order of magnitude the advantages coming from the high quality of the gamma beam. The proposed ELI-NP Array of Detectors (ELIADE) is made of 8 segmented clover detectors similar to those used in the TIGRESS array [22, 23] placed on two rings, one at 98 degrees and another at 135 degrees with respect to the photon beam direction. The current experimental setup considers the possibility of having the ring at 98 degrees slightly adjustable, so that it can also be used at 90 degrees.

Similar clover detectors are operational at TIGRESS since 2009, and they are already characterized and fully described in simulations [22, 23]. On one hand, this makes analytical calculations like those presented in the next section more reliable, as experimental data can be used for comparison. On the other hand, the specifics of the experimental setup at ELI-NP and the particular time structure of the gamma beam need to be taken into account.

Schematic representation of the experimental setup, as it is viewed from GEANT4 [24, 25] simulations is presented bellow. Figure 3 shows the ELIADE setup in the configuration that will be used for NRF experiments aimed at discovering the NRF signatures of nuclei of interest. This configuration is optimized for very accurate measurements, even at the cost of longer experiments: the target can be thin, and the measurements can rely on the segmentation of the detectors to deal with the Compton scattered photons from the target.

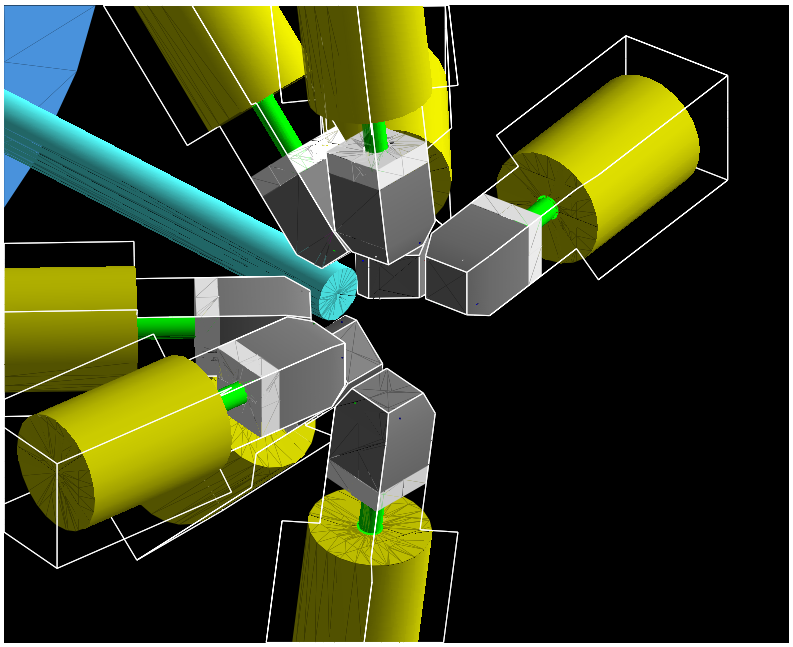

Fig. 3 – 3D rendering of the ELIADE setup.

For applications we are interested in obtaining the highest signal/noise ratio and an experimental time as short as possible. In the case of transmission experiments this translates into using a much thicker target at the centre of the ELIADE array (notch detector). In the case of scattering experiments, when the object of interest will be placed at the centre of the array the thickness is fixed by the object to be investigated. In both types of experiments we can expect a significant amount of Compton scattering from the gamma beam on the object in the centre of the array to reach the detectors. Assuming that the NRF signature of the nuclei of interest is already know, to reduce the impact of these events on the pile-up conditions in the detector we can use a passive lead filter which will have a much higher impact on the low energy Compton scattered photons than on the high energy NRF photons. Figure 4 shows a possible configuration of the ELIADE array where a thick (2 cm) Pb filter separates each of the detectors from the centre of the array.

The efficiency curves for this type of clover detectors were previously studied in Ref. [22]. In this study the clovers are used in a configuration using also anti-Compton detectors surrounding the cryostat. The impact of the lead filter on the absolute photo peak efficiency (assessed using our GEANT4 simulation of the Clover detector) and on the peak-to-total ratio using monoenergetic point sources for the high energy photons we expect from NRF resonances are shown in Fig. 5.

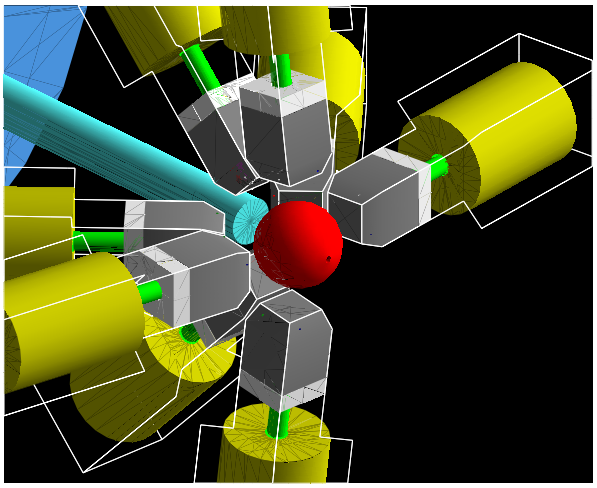

Fig. 4 – 3D rendering of the ELIADE setup with a thick Pb filter as the red ball object.

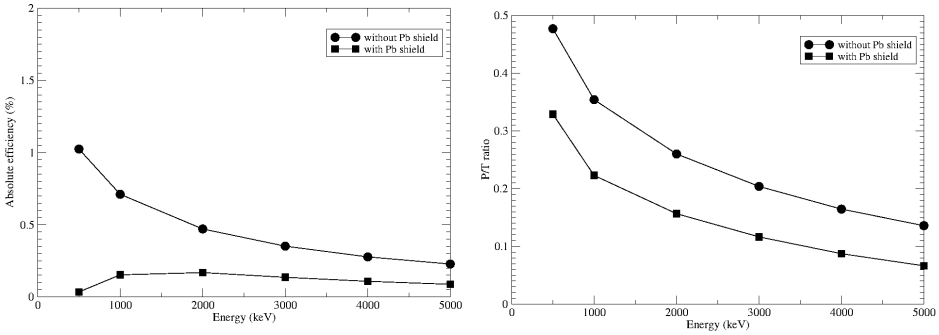

Fig. 5 – Performance (absolute efficiency and peak-to-total ratio) for a single segmented clover detector.

2.3.2. Analytical description of the background: Compton scattering and pair production from the target

The gamma beam of ELI-NP has some very specific characteristics. As a result of the electron beam structure and laser recirculation time at the interaction point the photons are emitted in very high intensity and in very short duration pulses. At design parameters, 10^8 photons are reaching the target each second, which are grouped in 100 macrobunches of 10^6 photons each. One macrobunch is made of 32 microbunches of a few ps length, separated by 16 ns. Even in the extraordinary bandwidth conditions of ELI-NP (0.5% of RMS energy), the number of photons within a typical nuclear resonance width (1 eV) is only of the order of 10^4 ph/s·eV. In these conditions, it is important to estimate the number of photons being scattered from the

target towards the detectors.

The two main processes that generate photons scattered in the target towards the detectors are the Compton effect and the pair generation in nuclear field. Other less studied processes like Delbruck, Nuclear Thomson and Nuclear Rayleigh, which might become important for certain nuclei, have been ignored in the analysis on the grounds of their low probability and the fact they were not shown to have a significant impact in previous NRF measurements. We will estimate the background coming from these effects considering a target of lead, 2 cm thick, which is one of the worst-case scenarios due to the high density and high Z.

A. Compton scattering

The angular distribution due to Compton scattering is given by the Klein-Nishina formula. Figure 6 shows the differential cross section in arbitrary units for the scattering of 3.5 MeV photons. The shape of the cross section remains roughly the same for the entire energy domain that we are interested in. In the graph, the vertical lines denote the angles covered by the two detector rings, one at 98 degrees (with an option to centre it on 90 degrees) and another one at 135 degree. The integrated cross section for the solid angle covered by the detectors is of about 5% of the total cross section for the ring at 90–98 degrees and of about 3% for the ring at 135 degrees (considering that each detector covers about 10 degrees in angle). The detailed values are given in the table 1 for several beam energies.

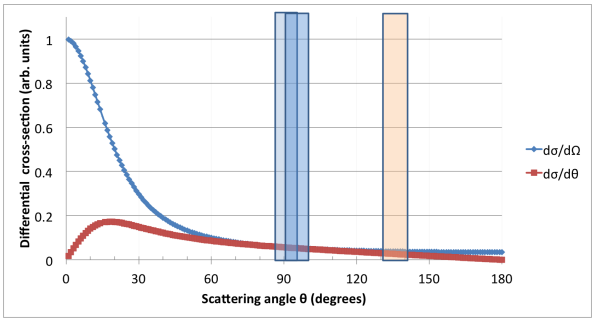

Fig. 6 – Example of Klein–Nishina cross section at 3.5 MeV. The vertical rectangles mark the angular positions of the detectors in the array.

The energy of scattered photons depends on the scattering angle. Because of the choice of angles, the scattered energy is very small compared to the energy of the incoming photons. Table 2 shows the expected scattered energy towards the center of each ring of detectors.

The interaction probabilities inside the Pb target are given by their respective cross sections. The values for the energies of interest in Pb are given in the table

Table 1

Integrated cross sections for several beam energies.

Energy (MeV)	ring at 90°	ring at 98°	ring at 135°
1	6.0%	5.5%	3.5%
2	5.6%	5.1%	2.9%
3.5	5.2%	4.7%	2.5%
5	4.9%	4.4%	2.3%
7	4.6%	4.1%	2.1%
10	4.4%	3.8%	1.9%

Table 2

The expected scattered energy for different incident beam energies.

Initial energy (MeV)	Scattered energy towards 90° (MeV)	Scattered energy towards 98° (MeV)	Scattered energy towards 135° (MeV)
1	0.33	0.30	0.23
2	0.40	0.35	0.26
3.5	0.44	0.38	0.27
5	0.46	0.40	0.28
7	0.47	0.40	0.28
10	0.48	0.41	0.29

below. As comparison, the integrated resonance at 2.1 MeV in ^{238}U is 0.19 cm^2/g·eV and it has a width of 1.78 eV.

Table 3

Photon cross section data for Pb

Energy (MeV)	Incoherent scattering (cm^2/g)	Nuclear pair production (cm^2/g)	Total (cm^2/g)
1	4.99×10^{-2}	0.00×10^{0}	7.10×10^{-2}
2	3.48×10^{-2}	5.45×10^{-3}	4.61×10^{-2}
3.5	2.49×10^{-2}	1.47×10^{-2}	4.19×10^{-2}
5	1.98×10^{-2}	2.15×10^{-2}	4.27×10^{-2}
7	1.57×10^{-2}	2.85×10^{-2}	4.53×10^{-2}
10	1.22×10^{-2}	3.67×10^{-2}	4.97×10^{-2}

Due to their low energy, some of the Compton scattered photons are absorbed in the lead filter that is being placed in front of the detectors. The effect of the lead

filter is shown in the Table 5 where it can be seen that for an attenuation of the high-energy photons by a factor of up to 5, the counts in the detector due to the Compton scattered photons decreases by up to 5 orders of magnitude. Two cases of shielding are shown to give an idea of how additional shielding impacts the rates in the detector.

Table 4

Transmission probability through Pb shielding as a function of energy

Energy (MeV)	2 cm Pb	2.5 cm Pb
0.23	8.04×10^{-8}	1.39×10^{-9}
0.30	1.07×10^{-4}	1.09×10^{-5}
0.35	1.20×10^{-3}	2.22×10^{-4}
0.40	5.15×10^{-3}	1.38×10^{-3}
0.45	1.34×10^{-2}	4.54×10^{-3}
0.50	2.58×10^{-2}	1.03×10^{-2}
1	2.00×10^{-1}	1.34×10^{-1}
2	3.52×10^{-1}	2.71×10^{-1}
3.5	3.86×10^{-1}	3.05×10^{-1}
5	3.80×10^{-1}	2.98×10^{-1}
7	3.58×10^{-1}	2.77×10^{-1}
10	3.24×10^{-1}	2.44×10^{-1}

Considering that the number of photons in one macrobunch is 10^6, the number of photons emitted towards the ring at 90 degrees is in the order of 10^4 low energy photons. A great part of these are absorbed in the lead shield, the remaining photons being detected by the clover detectors. The number of photons detected by each segment can be estimated from the table bellow by taking into account that the clovers only cover about half of the solid angle surrounding 90 degrees and that the low energy nature of these photons means that they are mostly detected in the front segments. As a result, the number of photons detected in each of these frontal segments for each macropulse is diminished by a factor: 2 (solid angle)$\times$4 (clovers)$\times$2 (crystals)$\times$4 (segments) = 64 of the flux after the shield. If the add-back procedure at clover level for the NRF photons takes into account the timing of the signals at microbunch level, then the background from Compton scattering has a very low impact on the overall measurement.

The situation is much better in the case of the detectors at 135 degrees, for which the rates due to Compton scattering in the target are almost negligible:

B. Pair production

The pair production process by the incoming photons in the target becomes more important as the energy of the photon increases, becoming as probable as the

Table 5

Statistics on the number of Compton scattered photons at 90 degrees and filtered by different thickness of Pb

Energy (MeV)	Incoherent scattering (cm^2/g)	σ / σ_{tot}	outgoing flux	flux after 2 cm shield	flux after 2.5 cm shield
1	4.99×10^{-2}	6.0%	3.10×10^{4}	3.6	0.4
2	3.48×10^{-2}	5.6%	2.49×10^{4}	140.9	37.8
3.5	2.49×10^{-2}	5.2%	1.70×10^{4}	253.0	86.0
5	1.98×10^{-2}	4.9%	1.25×10^{4}	188.5	64.1
7	1.57×10^{-2}	4.6%	9.15×10^{3}	138.2	47.0
10	1.22×10^{-2}	4.4%	6.36×10^{3}	186.4	74.7

Table 6

Statistics on the number of Compton scattered photons at 135 degrees and filtered by different thickness of Pb

Energy (MeV)	Incoherent scattering (cm^2/g)	σ / σ_{tot}	outgoing flux	flux after 2 cm shield	flux after 2.5 cm shield
1	4.99×10^{-2}	3.5%	1.94×10^{4}	0.0	0.0
2	3.48×10^{-2}	2.9%	1.40×10^{4}	0.0	0.0
3.5	2.49×10^{-2}	2.5%	9.01×10^{4}	1.0	0.1
5	1.98×10^{-2}	2.3%	6.47×10^{4}	0.7	0.1
7	1.57×10^{-2}	2.1%	4.62×10^{3}	0.5	0.1
10	1.22×10^{-2}	1.9%	3.16×10^{3}	0.3	0.0

Compton scattering in Pb around 5 MeV. The annihilation of the positron after slowing down in the target leads to the generation of two 511 keV photons emitted isotropically. We can simply obtain an estimate on the number of photons detected during each macrobunch using the known absolute efficiency and peak-to-total ratio for monoenergetic photons of 511 keV. In the case of the ELIADE, the absolute efficiency is around 8%, with a peak-to-total ratio of 0.3, leading to a total detection efficiency of 30%.

The number of photons detected by each segment can be estimated from the total number of detected photons by taking into account that all the segments of the array (8×4×8 = 256) are used for the detection. This leads to a high load on the detectors, load that can be significantly reduced either by reducing the target thickness, increasing the shield thickness and implementing the add-back procedure with timing at the microbunch level. For example, while the calculations here were

done for a 2 cm long Pb target, the NRF target used in the next example is reduced to 0.5 cm length, due to the high attenuation coefficient of resonant photons.

Table 7

Overview of the number of detected 511 keV photons for two shielding scenarios

Energy (MeV)	Nuclear pair production (cm^2/g)	Total outgoing flux	Transmission through 2 cm shield	Flux after shield	Detected photons	Transmission through 2.5 cm shield	Flux after shield	Detected photons
2	5.45×10^{-3}	76688	0.026	1977	593	0.010	792	238
3.5	1.47×10^{-2}	214399	0.026	5527	1658	0.010	2214	664
5	2.15×10^{-2}	311991	0.026	8042	2413	0.010	3222	967
7	2.85×10^{-2}	404450	0.026	10425	3128	0.010	4177	1253
10	3.67×10^{-2}	499267	0.026	12869	3861	0.010	5157	1547

In conclusion the experimental conditions at ELI-NP are difficult because of the background radiation being generated by the incoming photon beam in the target: Compton scattered photons and 511 keV photons generated through pair production. The calculations above show that using adequately thick Pb shields in front of the detectors, the number of these photons reaching the detector can be reduced by a few orders of magnitude to a level where a segmented detector can be employed without any significant pile-up within each segment even when the full macrobunch/microbunch beam is used. It should be noted that the background radiation is of low energy, meaning that it will be, with high probability, stopped in the frontal segments of the crystal. It should also be noted that the calculations above are for a thick 5 mm target, which would deplete almost completely the resonance photons. This allows another mechanism to reduce the background rate (and pile-up probability) by reducing the target thickness.

2.3.3. Analytical calculations

An analytical model to calculate the estimated NRF rates is described in [9] for both transmission and scattering experiments. For the case of scattering experiments the photon flux at the detector is described as the result of three components:

$$\Phi(r_d, E) = \Phi_{\mathrm{target}}(r_d, E) + \Phi_{\mathrm{radioactivity}}(r_d, E) + \Phi_{\mathrm{beam}}(r_d, E) \qquad (2)$$

where $\Phi(r_d, E)$ is the photon flux at the detector distance r_d and $\Phi_{\mathrm{target}}(r_d, E)$ is the contribution due to resonant and non-resonant scattering. Resonant scattering produces NRF signals where as the non-resonant scattering produces background. $\Phi_{\mathrm{radioactivity}}(r_d, E)$ is the contribution from decay inside the target and $\Phi_{\mathrm{beam}}(r_d, E)$ is due to interrogating beam photons that have reached the detector without interacting within the target material. Sufficient shielding must be placed between the

interrogating beam and the detectors to keep $\Phi_{\rm beam}(r_d, E)$ negligible.

A. Analytical description of the expected NRF counting rate

The rate at which the NRF signals due to photons of energy E, from a location, r, within the target volume, V , are detected is given by:

$$\frac{d^2R_{\rm NRF}}{dVdE} = N\Phi(E,r)\sigma_{\rm NRF}(E)W_e(\theta)exp(-\mu(E_\gamma)r_0)\left[\epsilon(E_\gamma)\frac{\Omega(r)}{4\pi}P_f(E_\gamma)\right] \quad (3)$$

where:

- N is the number density of atoms in the target that undergo NRF with cross section $\sigma_{\rm NRF}(E)$,
- $\Phi(E,r)$ is the energy-differentiated photon flux at the point r,
- $W_e(\theta)$ is the effective angular correlation function,
- E_γ is the energy of the emitted NRF ray, which interacts within the target material with an attenuation coefficient $\mu(E_\gamma)$, that results in a total attenuation of the NRF ray of $exp(-\mu(E_\gamma)r_0)$,
- $\epsilon(E_\gamma)$ is the probability that the radiation detector measures the full energy of the NRF ray,
- $\frac{\Omega(r)}{4\pi}$ is the fraction of the solid angle subtended by the radiation detector from the point where the NRF ray is emitted,
- $P_f(E_\gamma)$ is the probability that the NRF ray penetrates through the radiation filter without scatter.

All the parameters that appear in the formula are defined for a slab of material of thickness t as presented in Fig. 7.

Additional approximations are needed to simplify the formula:

- Neglect photon downscatter, so $\Phi(r) = \Phi(x)$; $\Phi(E,x) = \Phi_i exp(-\mu(E)x)$
- Neglect the energy dependence of photon absorption around resonance energy: $\mu(E) = \mu_{nr} + N\sigma_{\rm NRF}(E)$
- Consider the resonance cross section as constant for the width of the resonance: $\sigma_{\rm NRF}(E) = \sigma^C_{\rm NRF}$; $E \sim E_C$; $\sigma^C_{\rm NRF} = \frac{\int \sigma_{\rm NRF}(E)dE}{\Gamma_D}$

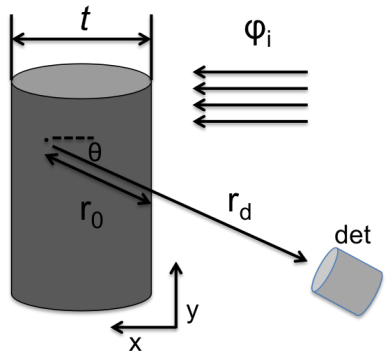

Fig. 7 – Schematic of the measuring geometry [9].

If we note: $\alpha = \mu_{nr}(1 + \frac{1}{cos\theta})$ then the NRF rate measured by the detector can be written as:

$$R_{\mathrm{NRF}} \approx \left[\frac{1 - exp[-(\alpha + N\sigma^{C}_{\mathrm{NRF}})t]}{\alpha + N\sigma^{C}_{\mathrm{NRF}}}\right][N\Phi_i\sigma^{C}_{\mathrm{NRF}}]\left[\frac{W_e(\theta)A\epsilon P_f(E_\gamma)}{4\pi r_d^2}\right] \quad (4)$$

If the three phenomena contributing to the rate are written separately then:

$$R_{\mathrm{NRF}} \approx [\mathrm{T}_1][\mathrm{T}_2][\mathrm{T}_3] \quad (5)$$

- T_1: Effective geometric attenuation of photons before and after NRF
- T_2: The rate at which NRF would occur in the target without attenuation
- T_3: The probability of detections of NRF photons emitted from the target. This term can be expressed as:

$$\mathrm{T}_3 = \mathrm{W_e}(\theta)\epsilon_{\mathrm{abs}}\mathrm{N_{det}}\mathrm{P_f}(\mathrm{E}_\gamma) \quad (6)$$

where ϵ_{abs} denotes the absolute detection efficiency by a single detector for the energy of the NRF photon emitted from the target and N_{det} represents the total number of detectors. The formula above can also be applied to estimate the measured rate from the witness foil in the case of a transmission experiment. The flux arriving at the witness foil undergoes attenuation in the target object:

$$\Phi(E) = \Phi_0(E)exp(-\mu(E)x) \quad (7)$$

which has two effects: the overall flux is decreased before the witness foil, and the number of photons in the resonance window is decreased proportionally with the number of resonant photons in the witness foil.

B. Transmission NRF experiment: comparison with similar experiment at HIγS

While the use of NRF for safeguards and nuclear waste management shows great promise, there are a few technical issues that need to be taken into account when choosing the test case for the initial estimate of the feasibility. The first point is that the information about the NRF resonances is not known for many nuclides of interest. Secondly, many of these materials have a special status in what concerns quantity and storage conditions, as well as in terms of manipulation. Also, it is desirable to have an estimate for one of the cases that can be measured as soon as possible after the commissioning of the experimental facility.

To address the most important issues, many of the experiments involving nuclear sensitive materials are performed using surrogate materials. We will follow the same course of action. The following numerical examples are given for the case of depleted Uranium (DU) used as surrogate for any of the actinides of interest and W or Pb as surrogate for the matrix in which these actinides reside.

The first estimate of rates can be done for the experimental conditions described in Ref. [5]. In this article, the photon beam delivered by HIγS is used in a transmission experiment, where the role of the object is played by a 1.3 cm slab of DU, shielded at times by a slab of 1.3 cm of W. The role of the notch detector is played by a thick DU target, followed by a Cu witness foil for beam normalization. Four high-purity-germanium HPGe coaxial detectors (60% relative efficiency) were positioned at backward angles relative to the beam and facing the witness foil location. Absorbers of 4 mm thick Cu and 4.5 mm of Pb were placed on the front face of each detector to reduce low energy background. Hagmann *et al.* [5] shows that the total number of NRF event is 110 in the most unfavorable case after 25.5 hours of measurement and concludes that a 6 hours measurement would be required for a six-sigma level detection of sensitive material in the object when using the 100 photons/eV·s flux at HIγS.

The table below presents the expected NRF rate estimated for the experimental conditions at ELI-NP. Each of the columns details the components of the analytical rate of detection of the NRF formula that was used in the calculation for one scenario. The scenarios evaluated in the calculations are, in the order of the columns:

I. No object (thickness of UO_2 and W shield set as 0). All incoming flux reaches the notch detector

II. 1.3 cm thick W shield is placed downstream of the detector

III. 1.3 cm thick UO_2 surrogate SNM material is placed downstream of the detector

IV. 1.3 cm thick W shield and 1.3 cm thick UO_2 surrogate SNM material are placed downstream of the detector, in a 'typical' scenario of hidden SNM

The number of photons used in the calculations (Table 8) is the estimated number of photons coming from the source within the 1.78 eV Debye width of the resonance, and using a conservative value for the spectral density of 2.8×10^4 photons/s·eV.

In conclusion, in the most unfavorable case, the same statistics as in the experiment at HIγS can be reached in less than two minutes. The three orders of magnitude difference can be roughly attributed to the two orders of magnitude difference in intensity and one order of magnitude from the detector array efficiency. It should be noted that the setup at ELI-NP considers that a 2 cm thick absorber is placed between the detectors and the notch target, to attenuate the low energy Compton background coming from the scattering on the target of the other photons in the beam, as opposed to the 0.5 cm used at HIγS.

2.3.4. NRF applications – Isotope Imaging

A high penetrability and a weak element dependence of attenuation coefficients of several MeV gamma-rays make possible to visualize density distribution inside a massive object by a technique of Computed Tomography (CT), which measures the transmittance of gamma-rays through objects. The CT technique will be discussed in detail in section 3. Besides, a distribution of nuclei of interest inside an object is also possible to be visualized by measuring NRF gamma-rays as described in section 2.1.

In this section we propose to use the transmission NRF method to obtain CT images of the isotope distribution inside objects. The attenuation of NRF events absorbed in the measuring object can be inferred from the NRF events from a notch target placed downstream. To examine the feasibility of the CT imaging of the specific isotope we made a simulation of the CT reconstruction of an isotopic (^{238}U) distribution in an object that consists of some dense materials using GEANT4 simulations.

A. Simulation setup

A simulation was performed using the GEANT4 Monte-Carlo simulation code. Since the NRF interaction is not included in the original GEANT4 code, a modified version of GEANT4, which takes into account all NRF processes, developed by our group [10], was employed in this work.

A schematic drawing of the simulation setup is shown in Fig. 8 [26]. The LCS gamma-ray beam comes from the left side of the figure. The gamma rays irradiate

Table 8

Expected NRF rates for experimental conditions at ELI-NP

	I	II	III	IV	Notes
E(MeV)	2.1	2.1	2.1	2.1	
UO_2(cm)	0	0	1.3	1.3	SNM
W(cm)	0	1.3	0	1.3	shielding
m(g) DU	1.88	1.88	1.88	1.88	notch
V(cm^3)	0.10	0.10	0.10	0.10	notch
Beam spot diameter(cm) [a]	0.5	0.5	0.5	0.5	
t(cm) [b]	0.5	0.5	0.5	0.5	
$\Phi_0(phot/s/\Gamma_D)$	50000	50000	50000	50000	beam
$\Phi_i(phot/s/\Gamma_D)$ [c]	50000	16755	388	130	
T_1	0.19	0.19	0.19	0.19	
μ_{nr}(cm^2/g)	0.05	0.05	0.05	0.05	
α [d]	0.91	0.91	0.91	0.91	
σ^C_{NRF}(cm^{-1}) [e]	3.74	3.74	3.74	3.74	
Γ_D(eV)	1.78	1.78	1.78	1.78	
t(cm)	0.5	0.5	0.5	0.5	
T_2	186832	62607	1451	486	
$\Phi_i(phot/s/\Gamma_D)$	50000	16755	388	130	
T_3	0.1	0.1	0.1	0.1	
W(θ)	1	1	1	1	
P_f [f]	0.36	0.36	0.36	0.36	
$\epsilon(\%)$ [g]	0.3	0.3	0.3	0.3	
N_{det}	8	8	8	8	
$\mathbf{R}_{\mathrm{NRF}}$ (counts/s)	311	104	2	1	

[a] Diameter of notch detector is the same as that of the beam

[b] Thickness calculated from the notch mass and beam diameter

[c] Incident flux of resonant photons on the notch target; The expected flux is extrapolated from the values in the table in Ref. [2], supplied by constructor

[d] Using a thin pin as a notch target, with detectors at 90°.

[e] The integrated cross section for the 2.1 MeV resonance in ^{238}U is 87 eV·b ([9])

[f] Due to a 2 cm thick Pb absorber around the target

[g] Conservative value. More details in the description of the setup section

the measuring object located on the beam axis. The object was rotated around a horizontal axis and moved vertically to obtain projection images. Downstream of the investigated object, a 25 cm thick lead wall was installed to protect the gamma-ray detector from radiation scattered from the object. The wall had a through hole on the beam axis for gamma rays, which were transmitted through the object. A notch target was located behind the wall. The notch target consists of pure ^{238}U and its thickness was 5 mm. The attenuation of gamma-ray at NRF resonant energy was measured by counting NRF gamma-rays from ^{238}U in the notch target. The detection system

consists of 16 HPGe crystals installed at 90 degree and 16 HPGe crystals installed at 135 degree. The diameter of the HPGe crystal was 6 cm and its length was 9 cm. In the actual ELI-NP spectrometer, each crystal will be segmented into 8 parts, but in this simulation each crystal was treated as one detector.

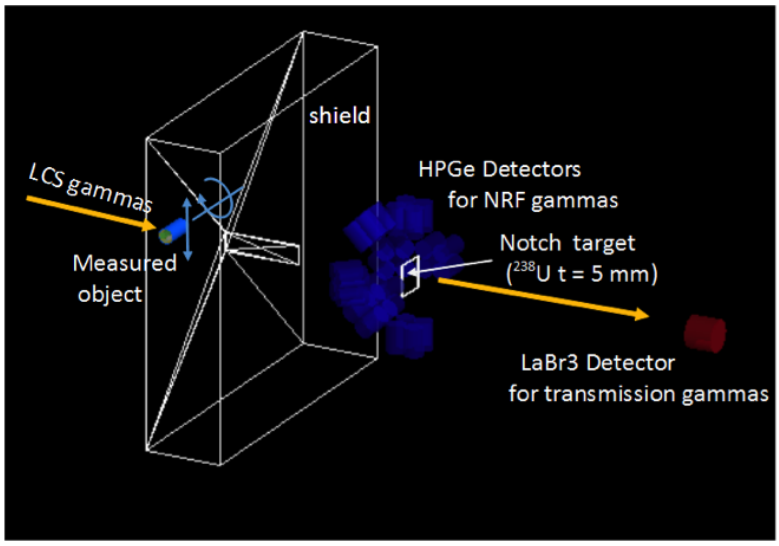

Fig. 8 – A schematic drawing of the target and detectors layout. LCS gamma rays come from the left side. A 25 cm lead wall protects the 32 HPGe detectors for NRF gamma-ray detection from radiations scattered from the measuring object. The penetrability of gamma-rays at the resonant energy of ^{238}U was measured by NRF gamma rays scattered on ^{238}U target located downstream of the lead wall. The attenuation of the whole gamma beam was measured by a $LaBr_3$ detector installed on the beam axis.

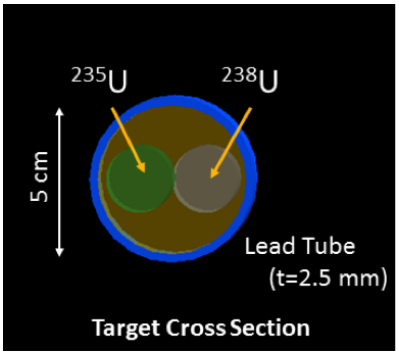

Fig. 9 – A cross-sectional view of the measured object. The outer diameter of lead tube is 5 cm and its thickness is 2.5 mm. Inside the tube, two 2 cm thick ^{235}U and ^{238}U rods are inserted and the tube is filled with gallium.

A cross section of a measured object is shown in Fig. 9. The object consists of a 5 cm outer and 4.5 cm inner diameter lead tube (density ρ = 11.34 g/cm^3, attenuation coefficient $\mu/\rho = 4.606 \times 10^{-2}$ g/cm^2) and 2 cm thick ^{235}U and ^{238}U rods (ρ = 18.95 g/cm^3, $\mu/\rho = 4.878 \times 10^{-2}$ g/cm^2). Between the tube and these rods, gallium (ρ = 5.904 g/cm3, $\mu/\rho = 4.113 \times 10^{-2}$ g/cm^2) was filled. In transmittance measurement of whole gamma-ray beam, the centroid energy of incident gamma-ray was 2176 keV which is equal to NRF resonant energy of ^{238}U and its energy spread was 0.5% in standard deviation which is the same as the ELI-NP specification. An incident photon number of 10^6 were considered for each measurement. This photon number is equivalent for the number of photons in one macrobunch. An attenuation factor was evaluated from a summation of energy deposit of all photon arrived at the $LaBr_3$ detector.

On the other hand, the fraction of gamma rays which energy is within a resonant width is only 10^{-4}. Thus, for attenuation measurement at NRF resonant energy, a monoenergetic gamma-ray beam was used to reduce the computation time. The incident photon number was equivalent for 100 sec. In the simulation, transmittance was measured at every 30 degrees (6 projection angles) by rotating the measured object and at every 1 mm (64 points) by scanning along the vertical direction. An energy distribution of gamma-rays detected by HPGe crystals is shown in Fig. 10. The two narrow peaks shown in the inserted frame are NRF peaks. The peak at higher energy is gamma-ray emitted by a transition to the ground state and lower one is to the first excited state (E_x = 44.9 keV). A broad peak at the foot of the higher energy peak is caused by elastic scattering on the notch target. The spectrum was obtained using a realistic ELI-NP gamma-ray beam energy profile and 2×10^9 incident photons [26]. The attenuation factor at NRF resonant energy was obtained from the yields of the narrow peaks. An example of the obtained projection image is shown in Fig. 11.

B. CT image reconstruction

CT image reconstruction was obtained using a filtered back projection method from 6 (one dimensional) projection images. The filter employed was the Shepp-Logan filter. The reconstructed images are shown in Fig. 12. In the figures, the large attenuation part is expressed with white. The left panel of Fig. 12 shows the density distribution obtained by whole gamma-ray attenuation factor, i.e. a standard CT image. The middle panel is reconstructed using the NRF yields. ^{238}U rod is clearly enhanced compared with ^{235}U rod. However, because of attenuation by other processes than NRF, other materials are visible also. These attenuations can be removed by evaluating the whole energy spectrum. The figure on the right panel represents the NRF yields normalized by the transmittance of whole energy gamma-ray. Consequently, we can clearly obtain an image of the ^{238}U rod and conclude that the

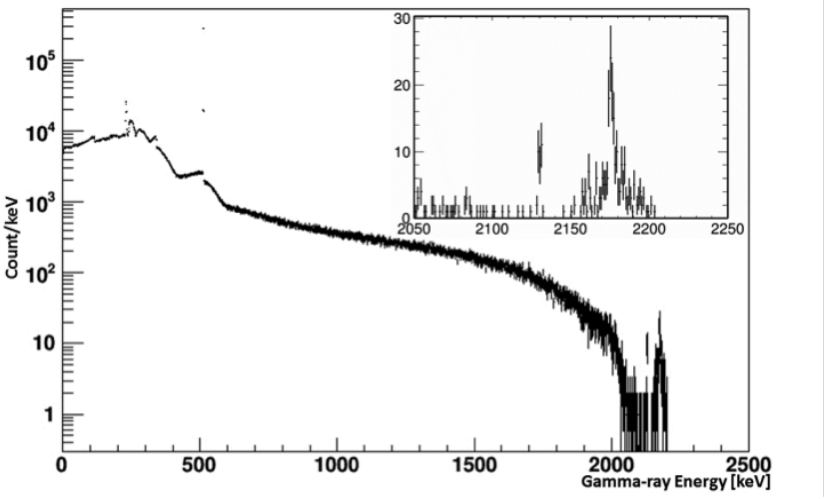

Fig. 10 – A typical energy spectrum obtained by HPGe detectors calculated by GEANT4. Inserted panel is an expansion around the NRF resonant energy. The two narrow peaks are gamma-rays from a nuclear resonance on ^{238}U.

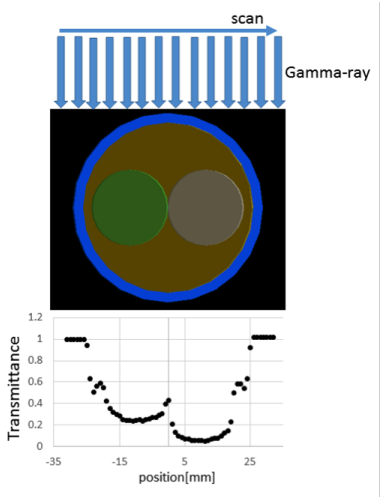

Fig. 11 – An example of NRF projection image obtained by scanning the measured object. By rotating the object, 6 projection images are obtained. The grey disk indicates the ^{238}U rod.

proposed method to visualize the isotope distribution could be feasible in the ELI-NP setup.

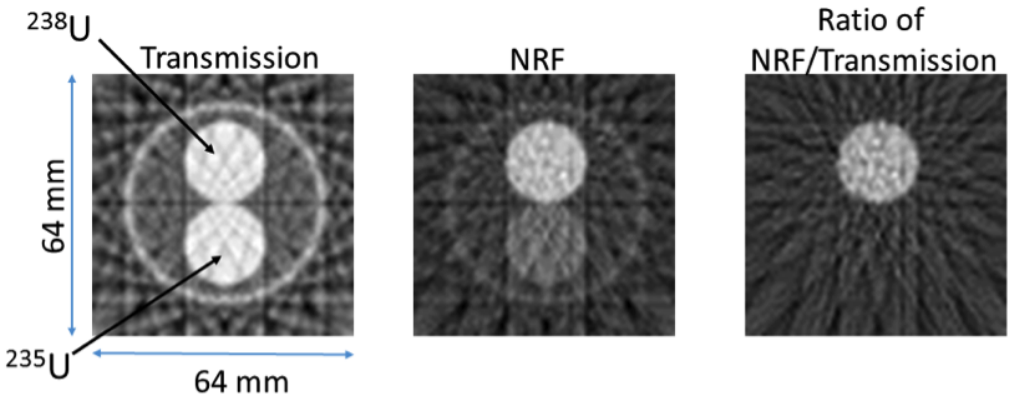

Fig. 12 – Cross-sectional images obtained by whole beam attenuation factor (left panel) and by NRF gamma rays (middle). Right panel image is reconstructed by the ratio of NRF gamma strength to transmittance of whole energy gamma beam. In the figures, the white parts are equivalent to strong gamma-ray attenuation sections.

2.4. TECHNICAL PROPOSAL

The NRF experimental setup will use the ELIADE array being developed for the dedicated NRF experiments. Its full description, location, mechanical support structure, vacuum, cooling and other requirements are detailed in the respective TDR. For scattering experiments, the object of interest will be placed at the target position of the ELIADE array. This can be used for small objects (distance between the detector face and centre of the array is between 15 cm and 25 cm). For transmission experiments, the notch detector will be placed at the centre of the array, and the object to be scanned on the tomography table, somewhere before the detector array.

3. RADIOSCOPY AND TOMOGRAPHY

3.1. INTRODUCTION

Radiography and tomography are imaging techniques that use ionizing radiation as an interrogation probe for medical or industrial purposes. Unlike radiography, which produces two-dimensional (2D) transmission images of 3D objects, computed tomography (CT) yields cross-sectional images that can be successively stacked up to create a 3D reconstruction of an object. Both methods are widely used in medical diagnostics nowadays using mainly X-rays or low energy gamma sources. In industry, gamma-ray CT had been mostly used in industrial columns/reactors to determine the phase distribution, phase separations and other non-uniformities inside two- or three-phase flow units [27–29]; an overview of the previous literature on computed tomog-

raphy used for industrial applications is published in Ref. [29]. Contrary to medical applications, usage of radiography and CT in industrial applications had limited applicability so far because industrial sized-objects require high-energy/high-intensity gamma beam for penetration [29].

With the new developments in the production of high-energy gamma beams by LCS technique, the interest in using CT tomography for industrial purposes had recently increased [18, 30]. Today there are several laboratories in the world that can produce high-energy gamma beams by the LCS and only few of these that can deliver high intensities as well [30, 31]. The future gamma source at ELI-NP will deliver both high-intensity and high-energy gamma beams being the perfect solution for industrial applications in tomography. The source beam intensity is with few orders of magnitude higher than any other gamma-ray source available increasing substantially the penetration length and respectively the maximum size of investigated objects. The quasi-monochromatic and high-intensity source characteristics allow acquiring an energy-selected data from the entire scattered and attenuated beam. For example, only by considering the small-angle scattered γ rays, a significantly improvement in image sharpness is obtained even for large-size and strongly scattering objects. In addition, the small beam width, allows achieving good resolution images for in-depth large objects technologies investigation, like: bonding in aeronautics, welding and machining accuracy in automotive industry, large concrete parts in constructions [30]. The γ-ray source with a tunable energy feature is very useful in adapting the energy range with the scanned object composition, for correctly revealing in the image the combination of different-attenuation materials, like plastic or ceramic with metals parts. Based on this feature, the dual/multi-energy technique could be also applied for scanning an object at different energies and obtaining information about its component materials like, for example, density and atomic effective number.

Based on the unique characteristics of the gamma-beam at ELI-NP we propose a Digital Radioscopy and Tomography (DRT) setup that will allow the investigation of industrial-sized object with high resolution and high contrast sensitivity. This setup will be specialized in non-destructive experiments and analysis by performing 2D transmission images and 3D reconstructed tomographs of the scanned objects, revealing the internal fine structure and composition, very useful in the development of processes for new technologies and materials and also for industrial complex structures analysis. Moreover, this setup may also be employed in performing isotope-specific imaging/mapping through the use of nuclear resonance fluorescence technique.

3.2. METHODS

To perform radioscopy and tomography at ELI-NP we propose a first generation tomography setup (pencil-beam) with a highly collimated beam. Toyokawa *et al.* [32] proved the working principle of a high-energy gamma-ray imaging system for industrial objects using a pencil-beam setup. They imaged several objects made of either low Z (concrete) or high Z (Pb, Fe, Cu) materials or a combination of the two [30, 32, 33]. The best spatial resolution attained using 10 MeV LCS photons was 650 μm, which was obtained using a 1 mm collimator placed after the object and a large (8 in x 12 in) NaI detector. Similar results were obtained at HIγS facility, where using a CCD-based gamma camera detection, they demonstrated a lateral resolution of 0.5 mm and a contrast sensitivity better than 6% [34]. At ELI-NP we expect to achieve a better spatial resolution and higher contrast sensitivity since the intensity of the ELI-NP gamma beam will be few orders of magnitude higher. More details about the performance of such setup will be presented in the following section.

Figure 13 shows a schematic view of the proposed DRT setup. A small-opening collimator placed after the object will define the beam width and the spatial resolution of the setup. In practice, usage of highly collimated beams is a trade-off between resolution and detection efficiency, therefore the targeted resolution for this setup is limited to sub-millimeter range. Nevertheless, in certain conditions (small or medium objects made of low Z materials) one can aim for a better spatial resolution that can reach up to 100–200 μm.

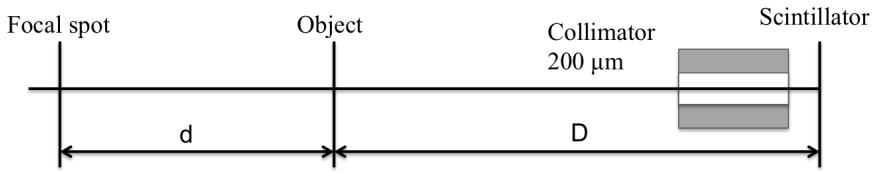

Fig. 13 – Schematic view of the ”pencil-beam” setup.

3.3. FEASIBILITY OF THE PROPOSED METHODS IN ELI-NP CONTEXT

In tomography an object is scanned along several directions (named projections) and an image of its cross section is obtained through image reconstruction. A collection of such 2D images (”slices”) measured along the height of the object can be used to construct a 3D view of the object. The performance of the DRT system depends on three parameters: spatial resolution, contrast and temporal resolution. The spatial resolution and the contrast are crucial parameters in scanning large industrial objects with high resolution, where as the temporal resolution is mainly important for

the investigation of dynamic processes. All three parameters are interrelated and affect the cost of the tomography setup so often a compromise is sought to achieve the best performance. The spatial resolution of a tomography system depends strongly on a few parameters, namely: the width of the beam, the number of projections and the number of detectors/projections. The contrast, i.e. the lowest measurable density difference, is greatly influenced by the intensity of the gamma beam and by the efficiency of detection. To study the feasibility of the proposed setup we rely on analytical calculations and numerical simulation in GEANT4 [24, 25].

3.3.1. Analytical calculations

To assess the performance of the DRT setup we estimate the spatial resolution and the contrast sensitivity using line-pair structures (line pairs per mm – LPM) [35]. In practice, we measure the contrast of a standard grid against the background provided by a homogenous object. Such a grid, made usually from stainless steel (SS) contains both linear and vertical bars. A diagram of such a grid is shown in Fig. 14. The thickness and the width of the bars are equal, and also equal with the spacing between two consecutive bars. The fact that we also vary the thickness of the bars allows us to determine the contrast sensitivity, not only the spatial resolution [30, 35]. For our estimates, the grid parameter, a, is varied from 2 mm to 0.1 mm corresponding to a resolution of 0.25 LPM to 5 LPM.

In the following, we present an analytical model for the pencil-beam tomography setup, which is used to estimate the resolution and the counting rates on the detector as well as the optimal parameters to be used in the simulation.

Figure 14 illustrates a schematic drawing of the experimental setup. The photons emitted from the interaction point pass through the ELI-NP collimator, leading to a highly collimated beam within the specifications (10^6 photons/macrobunch within 0.5% energy FWHM (full width at half maximum), see Ref. [2]). The photon beam then crosses the object, made in our calculations from a uniform object and a regular grid, and is then detected by a large size detector after passing through another collimator. The latter is used to define the beam width but also to reduce the scattered photons influence.

Depending on the size of the tomography collimator and of the distance between the detector and interaction point, the total number of photons coming from the source that reach the detector when the object is missing is given by:

$$I = I_0 \left(\frac{R_C}{D\theta} \right)^2 \tag{8}$$

where I_0 is the source intensity, R_c is the radius of the tomography collimator, D is the distance between the interaction point and the tomography collimator, and θ

is the angular opening of the source. In this calculation we assume that the main collimator is fixed and outside the scope of this TDR. Same assumption is made for the source. Another section will deal with improvements of the tomography setup, which can be attained by altering the beam properties and the "standard" opening of this collimator.

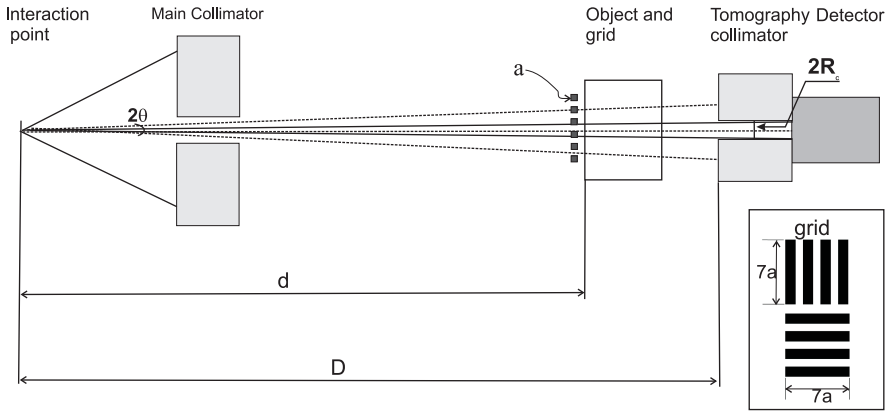

Fig. 14 – Schematic drawing of the experimental setup and of the grid used to assess the resolution.

As a result, in the first approximation, the source is:

- Monoenergetic: 0.5% FWHM is very small on the scale of the variation of the absorption coefficient
- Uniform: the density of photons within the solid angle is uniform

As we scan the beam across the grid, the number of photons reaching the detector will vary, increasing and decreasing as the beam intersects the grid or not. The number of photons reaching the detector when the beam passes between the grid bars is given by:

$$N_{\mathrm{MAX}} = Ie^{-\mu x}t\epsilon \tag{9}$$

where I is the available source intensity computed in equation (8), t is the acquisition time, ϵ is the efficiency of the detector, μ is the attenuation coefficient in the uniform object, and x is the object thickness.

The number of photons reaching the detector when the beam passes through the grid bar is given by:

$$N_{\mathrm{MIN}} = Ie^{-\mu_G a}e^{-\mu x}t\epsilon \tag{10}$$

where μ_G and a are the absorption coefficient of the grid and thickness of the grid. If we assume that the spot size of the beam reaching the detector at the grid position is smaller than the dimension of the grid bar then the beam reaching the detector will be modulated by the grid thickness. This can be written as:

$$\frac{R_C}{D} = \frac{fa}{d} \tag{11}$$

where f is a measure of how smaller the beam spot is compared to a. A small f will imply a finer scan but also a smaller diameter of the collimator, which will reduce greatly the intensity of the beam. If the beam spot at the grid is smaller or equal with a (i.e. $a > 2\theta d$) then the signal at the detector will be modulated by the grid, therefore no need for collimation.

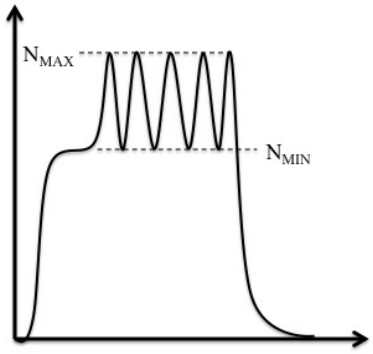

Fig. 15 – A drawing of generic signal.

In order to decide if the grid is visible or not in the scan data we need to compare the variation between N_{MAX} and N_{MIN} (Fig. 15). In practice, because of the small thickness of the grid we only expect few percent differences between N_{MAX} and N_{MIN}, so a serious issue is whether the differences are significant from the point of view of the counting statistics. To obtain good counting statistics in the detector we introduce the following conditions:

A.

$$N_{\mathrm{MAX}} - N_{\mathrm{MIN}} > S\sqrt{N}_{\mathrm{MAX}} \tag{12}$$

where S is a significance factor.

For S=2, the error bars of the two extreme points touch, so a higher contrast is given by a higher value of S.

We can write the equation for the time needed to attain a certain contrast S for a set of experimental conditions:

$$t = \frac{S_2}{e^{-\mu x}} \left(\frac{d}{fa}\right)^2 \frac{\theta^2}{I_0 \epsilon} \frac{1}{(1 - e^{-\mu_G a})^2} \tag{13}$$

B. Alternatively we can use: $N_{\mathrm{MAX}} - N_{\mathrm{MIN}} > S(\sqrt{N}_{\mathrm{MAX}} + \sqrt{N}_{\mathrm{MIN}})$

which leads to:

$$t > \frac{S_2}{e^{-\mu x}} \left(\frac{d}{fa}\right)^2 \frac{\theta^2}{I_0 \epsilon} \frac{1}{(1 - \sqrt{e^{-\mu_G a}})^2} \tag{14}$$

Based on the analytical model the main conclusions are: the object has to be as close to the source as possible and the measurement time scales with squared contrast S^2 and with $\frac{1}{a^4}$ for small a.

Numerical examples: Pencil-beam setup. To estimate the counting rates on the detector and assess the optimal resolutions and contrast sensitivity that we can achieve with the ELI-NP tomography setup we apply the analytical model for two experimental cases. For our estimates, the grid parameter, a, is varied from 2 mm to 0.1 mm corresponding to a resolution of 0.25 LPM to 5 LPM. The grid parameter a equals the width and the thickness of the grid bars as well as the separation between the bars. Therefore, the values cited in the following numerical examples represent not only the spatial resolution but also the contrast sensitivity attainable for a SS material.

Case 1. The setup is located after the low energy interaction point in experimental area E2. The attainable energies at this location are 3.5 MeV or lower, however the estimations are extended to higher energies as well for cases when the setup will operate at higher energies. For this numerical example we consider: $D = 40$ m, $d = 20$ m, $t = 1$ s, $\epsilon = 1$, $S = 10$, $f = 1/2$ (the "useful" diameter of the beam spot on the object is equal to a) and a stainless steel grid.

For the present case and according to equation (11) the collimator radius can be expressed as: $R_C = \frac{faD}{d} = a$.

Table 9 lists the thickness for several materials for which we can achieve a resolution of 0.7 mm ($R_C = 0.7$ mm) in the tomography using the parameters defined above and using equation (12) for the counting statistics. The rates/macrobunch (number of photons within the bandwidth per macrobunch) in the detector are listed in the table and are in the order of 10^3 photons. The maximum thickness of the investigated materials increases as we increase the energy of the gamma beam mostly because of the improved parameters of the gamma beam at high energy.

Table 9

Expected thicknesses for the case when the setup is after the low energy interaction point (case 1). The first three rows list the gamma source parameters as received from the manufacturer and used in the estimations (Ref. [2]).

Energy (MeV)	2	3.5	9.87	19.5
Source divergence (μrad)	140	100	50	40
Nr of photons within FWHM bandwidth	4.0×10^8	3.7×10^8	8.3×10^8	8.1×10^8
Al (cm)	30	41.2	88.9	104.9
Fe (cm)	10.4	13.5	23.7	24.3
H_2O (cm)	70.8	100.5	250.1	337.05
Concrete (cm)	33.8	47	106.8	131.6
Rates/macrobunch	1.9×10^3	2.9×10^3	3.9×10^3	3.4×10^3

Using the same analytical model we can estimate what is the highest resolution that we can achieve for certain materials and thicknesses if we limit the exposure time to 1 second. As one can see in the Table 10 one can obtain sub-mm resolution for all low Z materials listed up to 50 cm thick. For higher Z materials like Fe, sub-mm resolutions can be obtained only for small to medium size objects.

Table 10

Estimated resolutions achievable for different materials and thicknesses at beam energy of 3.5 MeV. Beam spot diameter is 4 mm at the sample and 8 mm at the collimator. The collimator has the inner radius equal to the resolution that we seek. Number of photons/s is 3.7×10^8 and the source divergence is 100 μrad.

Materials	10 cm	20 cm	30 cm	50 cm
Al	0.35 mm	0.44 mm	0.55 mm	0.85 mm
Fe	0.55 mm	1.09 mm	2.15 mm	4 mm in 20 s [a]
H_2O	0.31 mm	0.34 mm	0.37 mm	0.44 mm
Concrete	0.34 mm	0.41 mm	0.50 mm	0.74 mm

[a]The uncollimated beam spot is 4 mm at the object and this resolution can not be achieved in 1 s exposure time, only in 20 s

The values estimated in the tables are for large source-object distance (20 m), which represents one of the possible locations of the tomography setup in the experimental hall. Other possibilities for smaller object-distance exist as well and they will be listed in the ”location of the experimental setup” section. Smaller source-object distances are advantageous when higher resolutions are sought. Estimates for such a case are displayed below.

Case 2. For this numerical example we consider $D = 10$ m, $d = 5$ m, $t = 1$ s, $\epsilon = 1$, $S = 10$, $f = 1/2$ (the "useful" diameter of the beam spot on the object is equal to a) and a SS grid.

As has already been concluded from equation (13) and (14) we can improve the performance of the tomography setup by placing the object as close to the source as possible. In this configuration we can either reduce the measurement time for scanning similar objects as in the previous case or scan significantly larger objects. Table 11 lists the expected thickness of several materials for which we can achieve 0.7 mm resolution ($R_C = 0.7$ mm) at reduced source-object distance. The rates/macrobunch in the detector are in the order of 10^3 photons/macrobunch. Note that in the estimations for 9.87 MeV and for 19.5 MeV, the beam does not need any collimation (except to remove scattered radiation) since the beam spot at the object is 0.5 mm and 0.4 mm, respectively. At these two energies the estimated numbers are for a resolution of 0.5 and 0.4 mm, respectively.

Table 11

Expected thicknesses that can be scanned when the object is closer to the source (case 2). The rates per macrobunch are listed as well. The first three rows list the gamma source parameters as received from the manufacturer and used in the estimations (Ref. [2])

Energy (MeV)	2	3.5	9.87	19.5
Source divergence (μrad)	140	100	50	40
Nr of photons within FWHM bandwidth	4.0×10^8	3.7×10^8	8.3×10^8	8.1×10^8
Al (cm)	53.7	72.4	111.8	114.1
Fe (cm)	18.7	23.8	29.8	26.5
H_2O (cm)	126.9	176.4	314.3	366.8
Concrete (cm)	60.7	82.7	134.3	143.3
Rates/macrobunch	1.9×10^3	2.9×10^3	3.9×10^3	3.4×10^3

Table 12 lists the calculated optimal resolutions that can be achieved for different objects at high energies. The resolution depends on the collimator's inner radius according to equation (11). Therefore these resolutions are achievable using a collimator with an opening in radius equal to the resolution. As expected and also inferred from the tables, a smaller object-source distance will enhance considerably the resolution. Table 12 presents the estimated resolutions when using high-energy photons in case 2 example.

So far our estimates were done for exposures that last one second. The next tables (Table 13 and Table 14) lists the estimated measurement times (in seconds)

Table 12

Estimated sub-millimeter resolutions achievable for different materials and thicknesses at beam energy of 19.5 MeV in the case 2 setup. Beam spot diameter is 0.4 mm at the sample and 0.8 mm at the collimator. Number of photons/sec is 8.1×10^8 and the source divergence is 40 μrad.

Materials	10 cm	20 cm	30 cm	50 cm
Al	0.09 mm	0.10 mm	0.12 mm	0.16 mm
Fe	0.15 mm	0.27 mm	0.4 mm in 2.44 s [a]	0.4 mm in 380 s [b]
H_2O	0.080 mm	0.083 mm	0.087 mm	0.1 mm
Concrete	0.085 mm	0.095 mm	0.11 mm	0.13 mm

[a] The uncollimated beam spot is 0.4 mm at the object and this resolution can not be achieved in 1 s exposure time.

[b] same as note a

for one exposure when scanning 10 cm of material with two different resolutions: 0.2 mm (0.5% contrast) and 0.5 mm (1.23% contrast) using of 3.7×10^8 photons/s of 3.5 MeV energy. As expected the measurement times increase greatly for higher resolutions. Nevertheless, in case of a target resolution of 0.5 mm, the duration of one exposure is comparable with the macrobunch duration, i.e. 10 ms, for most of the low Z materials of 10 cm thickness (see Table 13).

Table 13

Estimated measurement times (in seconds) for one exposure when scanning an object of 10 cm with 0.2 mm resolution (0.5% contrast for SS at 3.5 MeV). The source-object (collimator) distance is 5 m (10 m).

Energy (MeV)	2	3.5	9.87	19.5
Source divergence (μrad)	140	100	50	40
Nr of photons within FWHM bandwidth	4.0×10^8	3.7×10^8	8.3×10^8	8.1×10^8
Al	0.90	0.575	0.066	0.036
Fe	7.97	3.54	0.369	0.250
H_2O	0.457	0.341	0.044	0.021
Concrete	0.784	0.515	0.059	0.032

These times are calculated for a geometry in which the source-object (d) source is 5 m and the ratio $D/d = 2$. Usage of other D/d ratio (magnification), can be scaled with the opening of the collimator (equation 11), hence no change in the measurement time, however at increased source-object distances, the measurement times for one exposure will increase accordingly (see equation (13)). These values are estimated using a single large detector with efficiency 1. In practice the efficiency of the

Table 14

Estimated measurement times (in seconds) for one exposure when scanning an object of 10 cm with 0.5 mm resolution (1.23% contrast for SS at 3.5 MeV). The source-object (collimator) distance is 5 m (10 m)

Energy (MeV)	2	3.5	9.87	19.5
Source divergence (μrad)	140	100	50	40
Nr of photons within FWHM bandwidth	4.0×10^{8}	3.7×10^{8}	8.3×10^{8}	8.1×10^{8}
Al	0.023	0.015	1.7×10^{-3}	9.3×10^{-4}
Fe	0.206	0.091	9.5×10^{-3}	6.4×10^{-3}
H_2O	0.012	8.8×10^{-3}	1.1×10^{-3}	6.2×10^{-4}
Concrete	0.020	0.013	1.5×10^{-3}	8.3×10^{-4}

detector is lower and the measurement times will vary with $1/\epsilon$.

Improvements of the tomography setup: Cone-beam setup. If the single detector is replaced by a 2D-array of detectors of small pixel size the total measurement time will be scaled with the total number of detectors, hence faster times and higher resolutions can be achieved in certain conditions. For such configurations, the gamma beam must have a larger divergence (cone-beam) with a beam spot at least equal to the area of the 2D detector. Such dedicated experimental setups are referred to as the fan-beam (linear array of detectors) or the cone-beam (2D-array of detectors) CT. In these cases, the targeted resolutions can reach 200 μm or better.

In the following we assess the feasibility of a cone-beam setup at ELI-NP. The main assumptions are:

- Increasing the opening of the main collimator leads to a greater divergence of the gamma beam and increase photon flux and bandwidth (for example, from preliminary data from EuroGammaS: 7×10^{9} photons/s for a 1mrad divergence)

- Detection is performed using a detector array, like a flat-panel detector, or a CCD camera device [34, 36].

In general, a flat panel detector consists of a high number of pixels with each pixel made of a small scintillator with limited thickness. So far on the market these pixels reach up to 1 mm in thickness for columnar CsI(Tl) scintillator plates [37, 38]. An important aspect when using flat-panel detectors for high-energy photons is the probability of interaction of photons in the scintillators, which in this case is lot smaller than 1.

The probability of interaction of photons in a scintillator (through all effects) is defined by:

$$p = 1 - exp(-\Sigma x) \tag{15}$$

where x is the thickness of the pixel and $\Sigma = n_1\sigma_1 + n_2\sigma_2$. The parameters: n_i and σ_i represent the number of atoms of the i-component in the scintillator per unit volume and the total cross section, respectively. For instance at 3.5 MeV photons the probability of interaction in a pixel of 500 μm for several scintillators is listed below and as expected is larger for higher density scintillators.

Table 15

Probability of interaction of photons of 3.5 MeV in a pixel of 500 μm thick.

Scintillator material	Density (g/cm^3)	p
BGO	7.13	0.0138
CsI(Tl)	4.51	0.0082
LSO	7.4	0.0139

In order to compare the two methods, pencil-beam and cone-beam CT, we compute the time needed to acquire a full scan of a small object by both methods. To calculate the total time we need first to define the total number of projections, named here P. The total number of projections has to fulfill the Nyquist-Shannon theorem:

$$P \geq \frac{\pi}{2} S \tag{16}$$

where S represents the number of sampling points in each projection line. $S = \phi/\Delta x$, for an object of diameter ϕ and for a sampling step Δx. Therefore the number of measurements needed to scan a 2D slice of an object, i.e to acquire a 2D cross-sectional image, is

$$M = P \cdot S = \frac{\pi}{2} \frac{\phi^2}{\Delta x^2} \tag{17}$$

If $\frac{h}{\Delta z}$ represents the total number of slices for an object of height h that is scanned with a z-axis-sampling step Δz, then we can define the total number of measurements needed to obtain a 3D reconstruction of an object as:

$$N = \frac{\pi}{2} \frac{\phi^2}{\Delta x^2} \frac{h}{\Delta z} \tag{18}$$

Then one can estimate the total measurement time required for the complete scan of an object as:

$t = t_1 N$ for a pencil-beam setup

$t = t_2 \frac{N}{N_{pixels}}$ for a cone-beam setup

where t_1 (t_2) is the time for a single exposure in the pencil-beam (cone-beam) and N_{pixels} represents the total number of pixels in the 2D-detector. For the cone-beam, the "single exposure time" expresses the estimated measurement time for a single pixel, i.e. considering only the fraction of the beam that falls on one pixel of the detector.

Next, we calculate and compare the time required to scan a small object through both methods: the pencil-beam and the cone-beam CT. The main assumptions are:

- Object: Aluminum (Al) cylinder of ϕ = 5 cm diameter and h =5 cm long ($\sim$0.26 Kg)
- Magnification D/d=2 (d=20 m)
- Cone-beam CT: source divergence is 1 mrad (beam diameter at object position is 40 mm and 80 mm at detector position); the 2D detector is as large as the beam spot and the pixel width is twice the resolution sought ($2a$)
- Pencil-beam CT: source divergence is 100 μrad (beam diameter at object position is 4 mm, and 8 mm at detector position); the detector is a large volume single detector, e.g. 30 cm of NaI. The pencil beam is obtained with a collimator that has an opening equal with twice the resolution sought ($2a$)
- E_γ = 3.5 MeV

Table 16 lists the estimates for the measurement times for single exposures, for measuring a single 2D slice with pencil-beam and the total time needed to scan a small object (5 cm $\times$ 5 cm) in cone-beam and pencil-beam CT. In addition the table also lists the number of photons per macrobunch that are "detected" in each case, considering a probability of interaction of 1 for the large volume detector (pencil-beam CT) and a probability of interaction of 1.6×10^{-2} for a 1 mm-thick pixel of CsI (cone-beam CT). It is noteworthy to mention that as long as the number of pixels in the detector is greater than the inverse of the interaction probability in the pixel, the cone-beam method is advantageous. Therefore the cone-beam method is useful when scanning objects with great detail (high resolution and high contrast sensitivity). However for cases when single 2D scans are required, the pencil beam is still advantageous. Note that this comparison between pencil-beam and cone-beam is carried out at low energies (3.5 MeV) where the source divergence is larger than at higher energies. In the latter case the smaller beam spots and the larger number of photons per second constitute advantages for the pencil-beam CT.

To summarize, the analytical calculations allow us to estimate the thickness of the materials that can be investigated in the DRT system at certain targeted resolu-

Table 16

Comparison between pencil-beam and cone-beam CT when scanning a small Al object (5 cm × 5 cm) with various resolutions at 3.5 MeV. CB=cone-beam; PB=pencil-beam; The probability of interaction in 1 mm-thick pixel of CsI is 1.6×10^{-2}

a (mm)	Pixel thickness (cm)	Nr. of measurements (N)	Nr. of pixels (pixel width)	Nr. of photons/sec	Single exposure time (s) [a]	Time for a 2D slice scan [b]	Total time for a 3D scan	$N_{detected}$/ macrobunch
1 (CB)	0.1	1.96×10^5	1.26×10^3 (2mm)	7×10^9	3.12 s		498 s	4.5×10^2
1 (PB)	30	1.96×10^5	1	3.7×10^8	0.01 s	39.2 s	1.96×10^3s	1.48×10^5
0.7 (CB)	0.1	5.74×10^5	2.56×10^3 (1.4 mm)	7×10^9	12.9 s		2952 s	2.2×10^2
0.7 (PB)	40	5.74×10^5	1	3.7×10^8	4×10^{-2} s	323 s	6.4 h	7.26×10^4
0.5 (CB)	0.1	1.57×10^6	5.03×10^3 (1mm)	7×10^9	49.3 s		4.36 h	1.1×10^2
0.5 (PB)	30	1.57×10^6	1	3.7×10^8	0.15 s	2376 s	66 h	3.7×10^4
0.2 (CB)	0.1	2.47×10^7	3.14×10^4 (0.4 mm)	7×10^9	1.9×10^3 s		417 h	1.8×10^1
0.2 (PB)	30	2.47×10^7	1	3.7×10^8	5.9 s	164 h	4.1×10^4h	5.9×10^3

[a] For the cone-beam, the "single exposure time" expresses the estimated measurement time for a single pixel, i.e. considering only the fraction of the beam that falls on one pixel of the detector. The time for a single exposure is estimated using condition (12) for S=10 to assure that we have enough statistics in each pixel of the 2D detector.

[b] The measurement time needed to scan a 2D slice of the object is computed for the pencil-beam only.

tions and calculate the expected detection times in order to have statistically significant measurements. There is a significant increase in the measurable thickness or resolution if higher energies are used due to the improved parameters of the gamma beam at these energies. When seeking higher resolutions a cone-beam may be advantageous under certain conditions mentioned above. As expected, large objects can be scanned with higher resolution at smaller source-object distances.

3.3.2. Numerical simulations

As was already mentioned in the previous section the analytical calculations are very useful in estimating detection rates and material's thicknesses that can be investigated. Nevertheless, to assess the feasibility of our proposed DRT setup we also rely on numerical simulations. The simulations are carried out in GEANT4 [24, 25] where we have implemented all the components of the experimental setup. The modeled gamma source has a size between 10–30 μm and a divergence between

25–200 μrad depending on the energy of the beam [2].

To test the spatial resolution and the contrast sensitivity of the tomography setup we simulate the transmission through various objects and grids using GEANT4. To estimate the optimal parameters to be used in the simulation we rely on analytical calculations. In practice, we measure the contrast of a standard stainless steel grid against the background provided by a homogenous object as pictured in Fig. 14 The scanning is done by moving the object and the grid by a fraction of a, where a represents the width and the thickness of the grid. The results of the simulation consist in either single line scans taken across the grid or in 2D-radiograph of the grid.

The spatial resolution and the contrast sensitivity of the tomography setup were firstly tested using water-based objects at low energies of the gamma beam. The water-based objects were used to mimic the attenuation in organic tissues. An example of a simulated 2D-radiograph of 5 mm grid is shown in Fig. 16. Because of the high number of exposures needed to simulate a 2D image of the entire grid we use a relatively low number of photons in the source (1×10^6) and a thick grid. For very thin grids (weak contrast) one needs a good counting statistics in the detectors hence a high number of photons in the source. In order to reduce the computational time we limit the number of the exposures by investigating the gamma transmission through the grid+object for single-line scans taken across the grid rather than 2D radiographs. Figure 16 illustrates single-line scans across a stainless steel grid of different widths/thicknesses. The grey boxes show the location of the grid bars. As one can clearly see, the grid is distinguishable even for 0.25 mm width/thickness. This high resolution is possible due to the small opening of the tomography collimator used, which is 0.2 mm in diameter and thanks to the low attenuation in the object.

In the pencil-beam configuration, the degree of collimation of the beam defines the spatial resolution of the setup. Highly collimated beam imply lower beam intensities, hence a compromise must be reached between spatial resolution and detection efficiency. Figure 17 presents the simulated grid profile of 0.38 mm grid placed in front of an Al object for different opening of the collimator (R_C) located at 10 m from the source ($D/d = 2$). Thickness of the Al object is varied to obtain similar counting statistics in the detector (Table 17). The simulation results indicate that in order to maximize the counting statistics for a given resolution, the size of the collimated beam (see equation (11)) can be as large as aD/d , i.e. $f = 1/2$. In our particular case studied here, the collimated beam diameter is twice the resolution sought ($D/d = 2$).

To validate our simulations we compare them with analytical curves. Figure 18 presents the results of the tomography simulations for an Al object of 10 cm thickness. This object was scanned with 2.3×10^7 photons at energy of 3.5 MeV $\pm$ 17 keV in a geometry similar to that described by case 1 in section 3.3.2. (source-

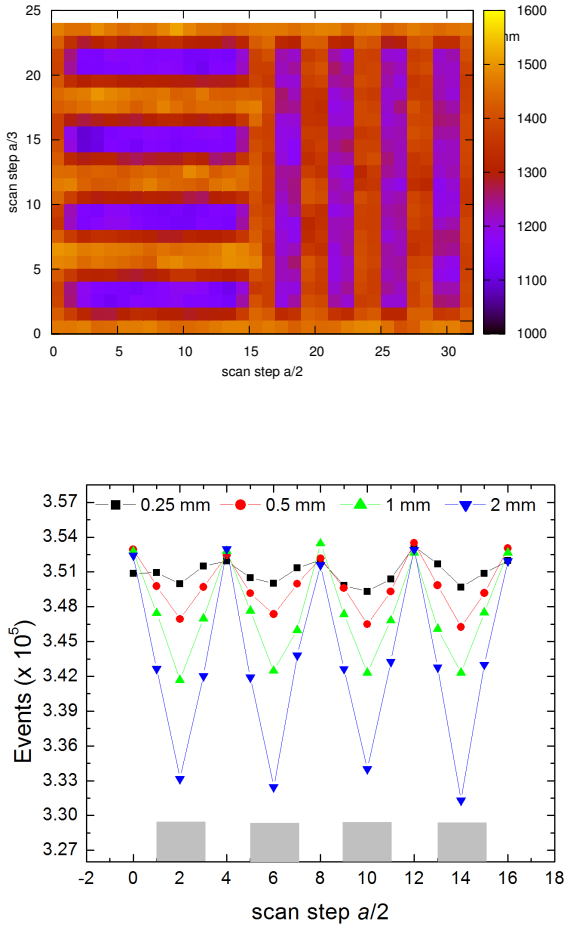

Fig. 16 – Number of 2 MeV photons that reach the face of a detector after passing through a 10 cm water-based object and a grid of variable thickness/width. The left panel presents a 2D-radiograph for $a = 5$ mm grid and the right panel shows single-line scans for several grid dimensions. The source had 1×10^6 photons in the left panel and 1×10^8 photons in the right panel. The color scale reflects the number of photons that reach the detector. The source-object distance is 5 m, the magnification is 2.

object distance of 20 m with magnification 2). The transmitted beam was collimated using a collimator with an inner radius of 0.7 mm, an outer radius of 10 cm and 20 cm long. A good agreement between the analytical model and the simulation is obtained with a systematic difference of 3% in the intensity at the detector.

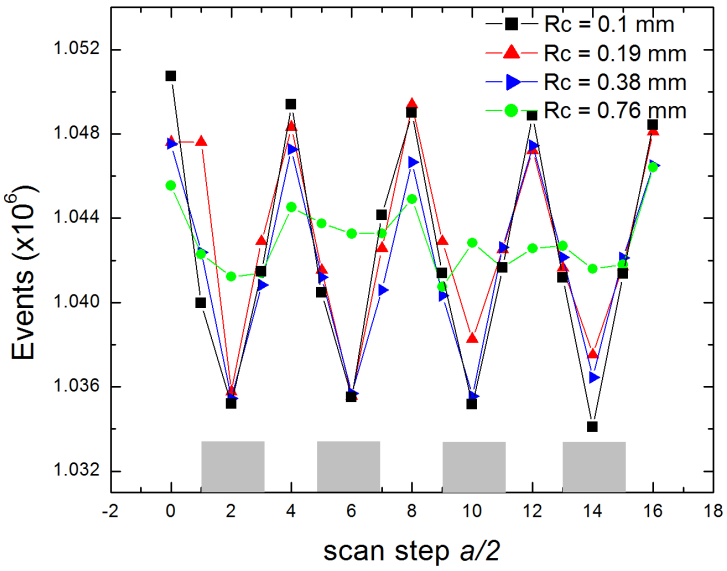

Fig. 17 – Number of photons that reach the detector after passing through an Al object and a 0.38 mm SS grid for different collimated beams at E_γ=3.5 MeV. The grey boxes show the location of the grid bars.

Table 17

Maximum thickness measurable with a resolution of 0.38 mm (1% contrast) at 3.5 MeV for different collimated beams. The source used has 1×10^8 photons. The source-object (-collimator) distance is 5 m (10 m). Assuming a beam divergence of 100 μm, the diameter of the beam spot at the sample is 1 mm and 2 mm at the detector. Through further collimation the beam spot at the sample can be reduced according to equation (11).

f	R_C (mm)	Al(cm)	Concrete (cm)	Fe (cm)
0.137	0.1	1.2	1.4	0.4
0.25	0.19	14.74	16.82	4.84
0.5	0.38	30.33	34.61	9.97
1	0.76	45.92	52.41	15.09

3.4. CT RECONSTRUCTIONS

An important and crucial part of the computed tomography is the image reconstruction process. Using mathematical algorithms a 3D image of an object can be reconstructed from its projections.

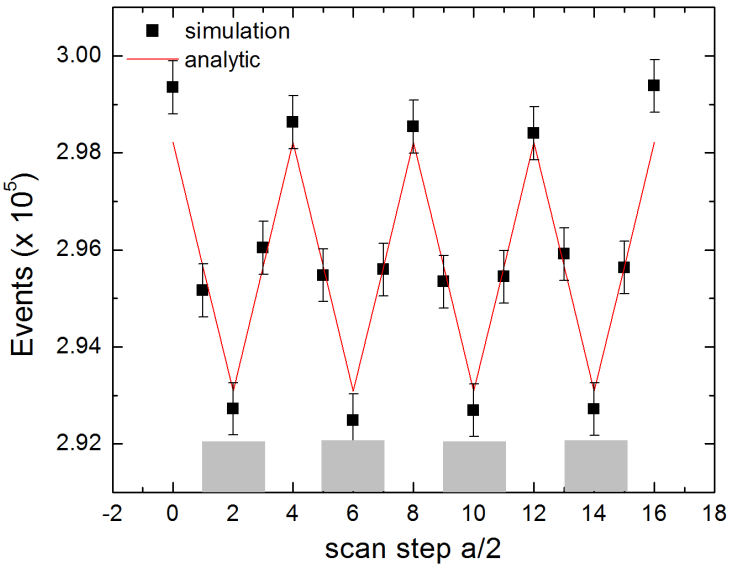

Fig. 18 – Comparison between the Monte Carlo simulated and the calculated number of transmitted photons using the analytical model. The object is an Al cylinder of 10 cm thickness in the beam. The gray boxes show the location of the grid bars. The grid bars are 0.7 mm in width and thickness. The analytical curve was vertically displaced upwards (corrected with the 3% difference) to overlap the simulation data. The error bars represent the squared root of the number of events.

Figure 19 presents the reconstructed CT images of simulated data. The object is a cylinder of 45 mm diameter with walls of 2.5 mm thick that is made of a material that has the linear attenuation coefficient 0.5 cm^{-1}. The cylinder is filled with a liquid having μ = 0.2 cm^{-1} and contains a heavy metal (μ= 0.9 cm^{-1}) rod inside. For the simulations we use 500 detectors placed in a linear array. The high number of detectors implies a resolution as low as 90 μm. The number of projections needed to reconstruct a 2D-cross-sectional image of this object is 785 according to the Nyquist-Shannon theorem. Figure 19 shows the simulated CT reconstructions as a function of the number of projections. Note that a good quality image can also be obtained with half the estimated number of projections. The CT reconstruction is done using the filtered-back projection algorithm together with a Sheep-Logan filter. We calculated the signal to noise ratio for each tomography to emphasize the higher quality of the image when using larger number of projections.

Measurement time estimations for obtaining a 2D cross-sectional image considering the expected ELI-NP gamma-beam capabilities are listed in Table 16 for a

similar size object, using pencil-beam CT. Note that depending on the complexity of the object good quality images can be obtained with smaller number of projections.

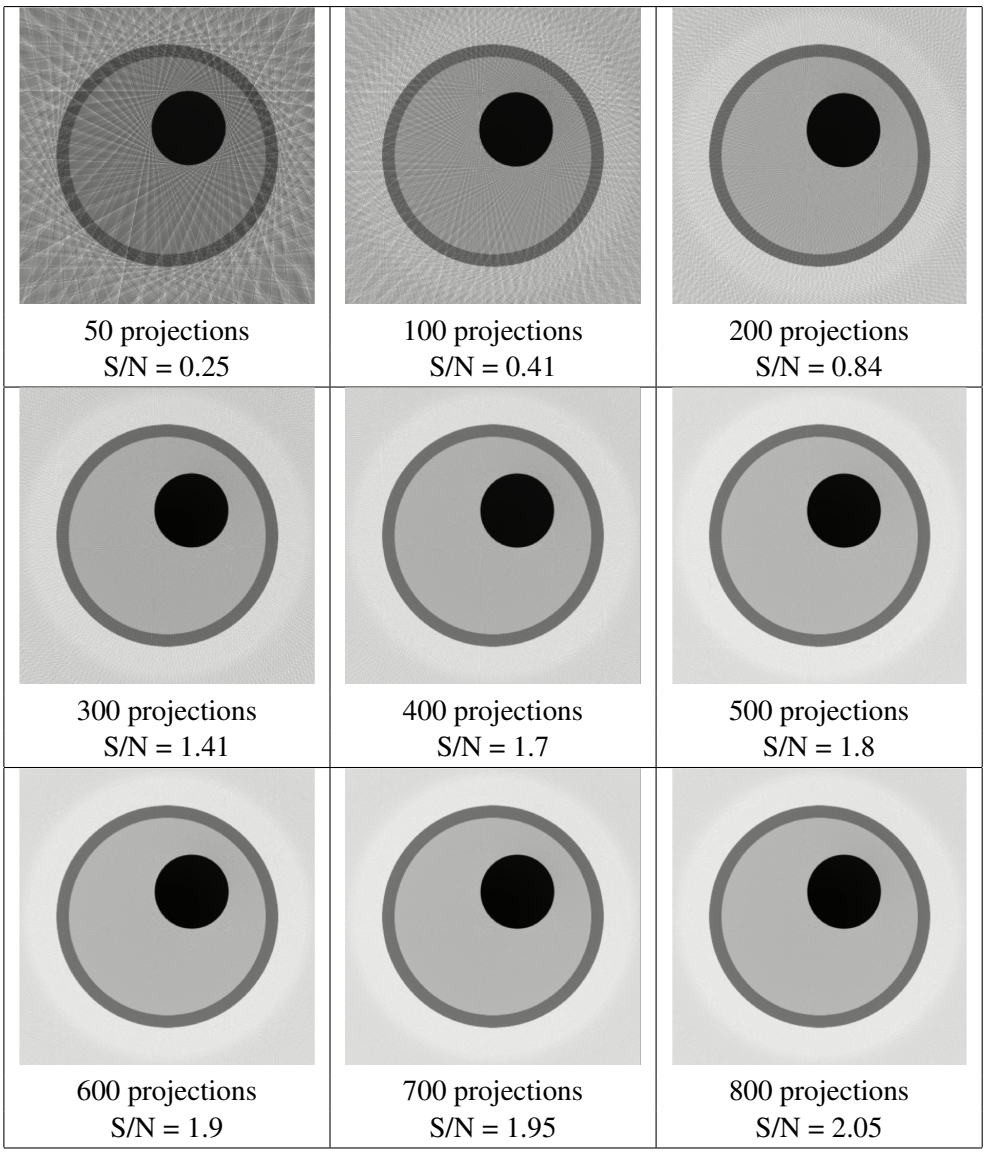

Fig. 19 – CT reconstructed images of simulated data. The number of projections used and the signal to noise ratio (S/N) are specified below each image.

3.5. TECHNICAL PROPOSAL

Figure 20 illustrates a diagram of the pencil-beam DRT setup proposed at ELI-NP. The main components are labeled in the figure and their detailed description will follow. The picture depicts a particular geometry for the case of large-object investigations however there is flexibility in adjusting the geometrical parameters for smaller sample investigations. The geometrical and spatial parameters will be presented in the section dedicated to the location of the experimental setup. Figure 21 illustrates the diagram of the 2D-high energy gamma detector that can be used for cone-beam tomography.

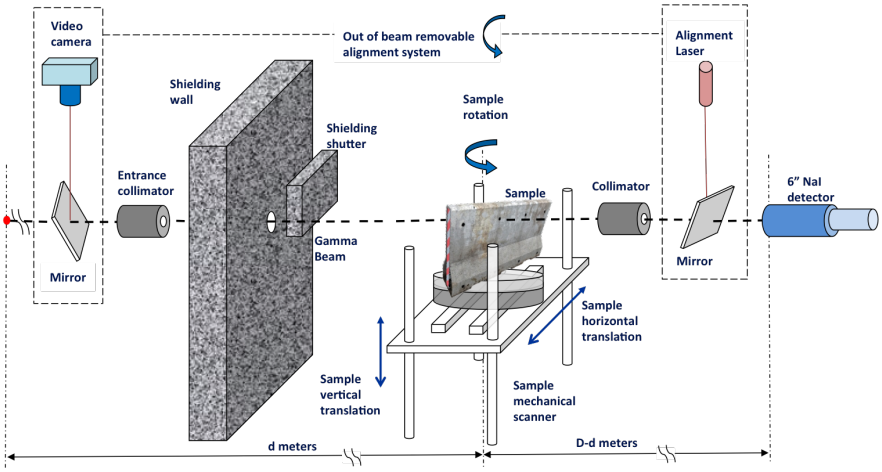

Fig. 20 – Digital radiography and tomography pencil-beam gamma-ray setup for large-size samples for industrial applications.

3.5.1. Location of the experimental setup

So far in the estimations we have used two examples for the setup geometries, one at low energies and one at high energies. In practice, at low energies we have up to 60 m for placing the object and the detector. This 60 m is roughly the length of the 2nd part of the accelerator, leading to the second interaction point. While we also show the numbers for the high-energy gamma beam, we worked under the assumption that the tomography setup will first be placed at the low-energy point so that we can start measuring from the start of the machine operation. Once the high-energy beam will be available, we can move equipment there based on space limitation.

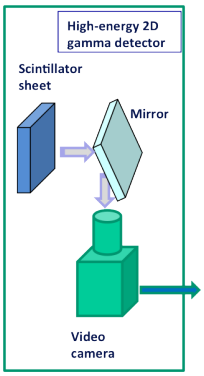

Fig. 21 – Schematic diagram of the high-energy 2D gamma detector for cone-beam CT.

3.5.2. Sample positioning system

The sample positioning system will consist of two tomography tables (one large and one small) to be used in different locations of the laboratory to be in agreement with the space and the weight limit. One table will be dedicated to large and heavy objects while another will be dedicated to small and light objects. The characteristics of the two tables are listed below.

- X- (Y-) axis travel: 1500/150 mm
- Z-axis travel: 2000/250 mm
- Max load: 150/10 Kg
- Positioning resolution: 10 μm, 0.05 $^\circ$ (30 μm, 0.1 $^\circ$)
- Speed: between 0.1 mm/s and 5 cm/s, with programmed ramps, speed accuracy: 0.5%

In addition to the tables, the setup needs the following components:

- Position sensors for all axes
- Feedback DSP based real-time positioning and speed control.

3.5.3. Collimators

The feasibility study indicated that a high degree of flexibility is needed in choosing the opening of the collimator in order to maintain a high speed for scanning objects as well as a good counting rate in scanning large objects. Therefore to gain such versatility a variable opening collimator from 0.1 mm to 3 mm will be optimal.

However due to the complexity of such collimator and its high price at the beginning we will use sets of individual collimators. The collimators will be made of lead (Pb) or tungsten (W) with various collimation holes: 100 μm, 200 μm, 500 μm, 700 μm, 1 mm, 3 mm, 6 mm. The collimators will need mechanical supports and alignment tables equipped with X, Y and Z scale-movement and rotation.

3.5.4. Detectors for the DRT setup

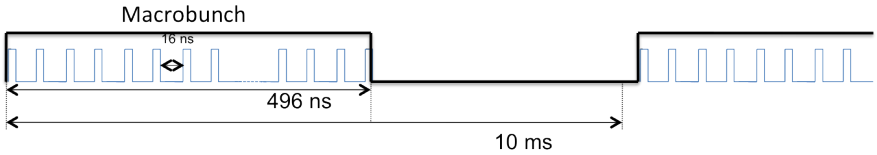

Fig. 22 – Time structure of the gamma beam. A macrobunch consists of 32 micropulses, which repeat every 16 ns. The repetition rate for macrobunches is 100 Hz.

The rates per macrobunch in the detector for a tomography experiment were estimated to be between 100 and 10000 photons/macrobunch depending on the gamma-beam energy, the object thickness and the source-detector distances. Such high rates of high-energy photons represent an outstanding challenge for detection complicated even more by the peculiar time structure of the beam (Fig. 22). At high photons energies, detectors based on scintillator crystals are more practical than any other detectors because of their high efficiency. The characteristics of some common scintillators are present in Table 18. The ideal choice of a detector for the pencil-beam setup would be a scintillator with high stopping efficiency; however a large NaI(Tl) (8 in $\times$ 12 in) would fulfill same requirement and could represent a good choice to start with as is often used in tomography setups. Another choice may be a $LaBr_3$ scintillator for cases when the transmitted gamma beam is too intense and would cause significant pile-up in the detector. Since the $LaBr_3$ has the shortest decay time (comparable with the microbunch time interval) it may help avoid or at least reduce the pile-up events. In case of the cone-beam measurements, a flat-panel detector, or a CCD camera-based device can be considered. A CCD-based imaging device consists of a scintillator plate that converts the incident radiation into visible photons and a CCD camera that detects them [34]. The advantage of using a CCD camera-based device over the single radiation detector stands in its relatively small pixel size (down to tens of micrometers). In addition, for high-energy photons we may consider a CdTe flat-panel detector. For the isotopic measurements that combine CT tomography with NRF based detection, we will use the transmission NRF method and its detector system described in section 2.

To overcome the issue of high number of photons/macrobunch we will use a

Table 18

Scintillator characteristics

Detector	NaI(Tl)	CsI(Tl)	BGO	LSO	$LaBr_3$
Density (g/cm3)	3.67	4.51	7.13	7.35	5.29
L_{rad} (cm)	2.59	1.85	1.12	0.88	2.1
Decay time (ns)	230	1000	300	40	16
Light yield (photons/keV)	38	54	8-10	25	63
Luminescence (nm)	410	530	480	420	380
Hygroscopic	Yes	Slightly	No	No	Yes

photomultiplier (PMT) with adjustable gain over a large range (few orders of magnitude). For example R1250 PMT from Hamamatsu has a voltage adjustable gain that spans over 6 orders of magnitude.

3.5.5. Electronics and DAQ

Figure 23 presents a schematic of the electronics and interconnections required for operating a DRT setup. The three main components of the diagram are: the sample positioning system, the movement control system and the data acquisition systems.

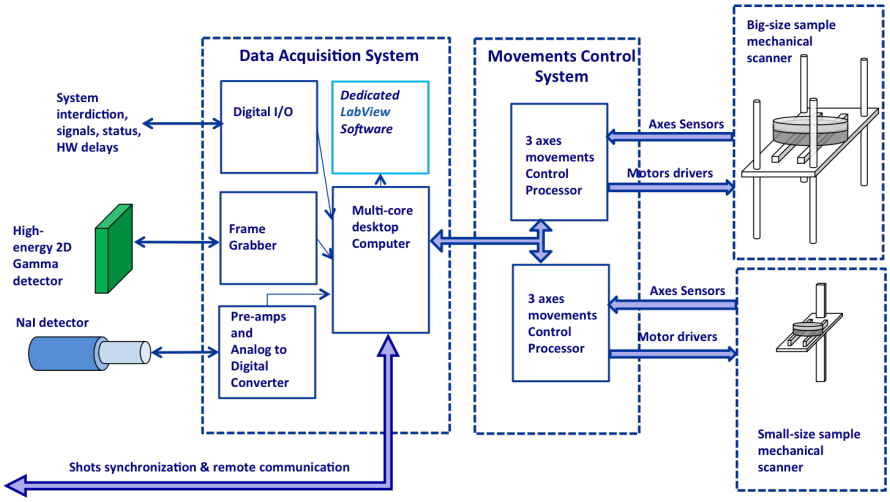

Fig. 23 – Schematic of the electronics and interconnections.

3.5.6. The mechanical support structure

The mechanical support structure for the translation tables will consist of a stack of three one-directional tables. Because they are general-purpose objects, their detailed design depends on the precise implementation by the producer and hence is dependent on results of the tender procedure. ELI-NP will only design the coupling between the tables and ensure their proper placement inside the experimental hall.

The support structure for the detectors and collimators is a simple one, with the detectors and collimators being aligned with the beamline using the global network of reference points.

3.5.7. HV and LV power supplies

The voltage requirements of the setups require general 220 V, 50 Hz power connectors. The HV for the scintillator detectors will be supplied by NIM modules inside a crate. The power supplies for the low-load table will be most likely of low voltage DC (24 V - subject to manufacturer specifications) while for the high-load table will be probably 220 V AC (subject to the manufacturer specifications).

3.5.8. Cabling

The DRT setup will use cables of various types and length to interconnect:

- The small and big table components with PC and Movement Controllers
- PC with Movements Controller, Detectors and Gamma Beam Control Room
- The setups in the experimental hall with the general data stream and controls of ELI-NP.

4. SPECIFIC NEEDS AND UTILITIES, TRANSVERSAL NEEDS

The implementation of this TDR will rely on the available ELI-NP infrastructure: electronic and mechanical workshop; clean room for detector assembly and storage; high speed 10Gb/s Ethernet or Infini band data connections from experiment to control/data acquisition room; high speed data storage system; radioactive sources for detector testing and calibration; clean power supply lines; clean grounding connections.

5. COLLABORATIONS

A memorandum of scientific collaboration exists with: The Institute of Advanced Energy, Kyoto University, Japan and ACCENT PRO 2000 s.r.l. Bucharest,

Romania.

Acknowledgements. The ELI-NP project is co-funded by the European Union through the European Regional Development Fund. The authors would like to acknowledge the help received from the engineering bureau, especially from Cristian Petcu and Emil Udup.

REFERENCES

1. Extreme Light Infrastructure-Nuclear Physics White Book, url: http://eli-np.ro/documents/ELI-NP-WhiteBook.pdf
2. O. Adriani *et al.*, Technical Design Report EuroGammaS proposal for the ELI-NP Gamma beam System, arXiv:1407.3669 (2014).
3. W. Bertozzi and R. J. Ledoux, Nucl. Instr. and Meth. Phys. Res. B **241**, 820 (2005).
4. G. Warren, J. Caggiano, and P. Peplowski, AIP Conference Proceedings **1194**, 106 (2009).
5. C. A. Hagmann *et al.*, J. of Appl. Phys. **106**, 084901 (2009).
6. D. L. Chichester, Industrial applications of photonuclear resonance excitations, Thesis 2000, url: http://dspace.mit.edu/handle/1721.1/29298
7. R. Hajima, T. Hayakawa, N. Kikuzawa and E. Minehara, J. Nucl. Sci. Tech. **45**, 441 (2008).
8. J. Pruet, D. P. McNabb, C.A. Hagmann, F.V. Hartemann, and C. P. J. Barty, J. Appl. Phys. **99**, 123102 (2006).
9. B.A. Ludewigt, B. J. Quiter, and S.D. Ambers, Nuclear resonance fluorescence for safeguards applications, DOE report, url: http://dx.doi.org/10.2172/1022713 (2011).
10. H. H. Negm, Studies on the optimum geometry for a nuclear resonance fluorescence detection system for nuclear safety applications, Thesis, Kyoto University (2014).
11. N. Kikuzawa *et al.*, Appl. Phys. Express **2**, 036502(2009).
12. T. Hayakawa *et al.*, Rev. Sci. Instr. **80**, 045110 (2009).
13. B. J. Quiter, Nuclear resonance fluorescence for nuclear materials assay, Thesis, url: https://escholarship.org/uc/item/0kc2s2kn, Univ. California, Berkley (2010).
14. B. J. Quiter, B. A. Ludewigt, V. V. Mozin, and S. G. Prussin, IEEE Trans. on Nucl. Sci. **58**, 400 (2011).
15. O. Beck *et. al.*, J. Appl. Phys. **83**, 5484 (1998).
16. CODEX General Standard for Contaminants and toxins in food and feed, Codex Standard 193-1995 (1995).
17. M. N. Lakshmanan, B. P. Harrawood, G. A. Agasthya, A. J. Kapadia, IEEE Trans. On Med. Imag. **33**, 546 (2014).
18. H. Toyokawa *et al.*, Jap. J. of App. Phys. **50**, 100209 (2011).
19. D. Vartsky, K. J. Ellis, D. M. Hull and S. H. Cohn, Phys. Med. Biol, **24**, 689 (1979).
20. L. Wielopolski, R. C. Ancona, R. T. Mossey, A. N. Vaswani, and S. H. Cohn, Med. Phys. **12**, 401 (1985).
21. H. Yang, Active interrogation methods for detection of special nuclear material, Thesis, url: http://hdl.handle.net/2027.42/64778 (2009).
22. M. A. Schumaker and C.E. Svensson, Nucl. Instrum. and Meth. Phys. Res. A **575**, 421 (2007).
23. M. A. Schumaker *et al.*, Nucl. Instrum. and Meth. Phys. Res. A **570**, 437 (2007).
24. S. Agostinelli *et al.*, Nucl. Instr. Meth. Phys. Res. A **506**, 250 (2003).
25. J. Allison *et al.*, IEEE Trans. Nucl. Sci. **53**, 270 (2006).

26. I. Daito, H. Ohgaki, G. Suliman, V. Iancu, C. A. Ur, M. Iovea, Simulation study on computer tomography imaging of nuclear distribution by quasi monoenergetic gamma rays with nuclear resonance fluorescence: case study for ELI-NP application, to be published in Energy Procedia.
27. S. Boden, M. Bieberle, and U. Hampel, Chem. Eng. J. 139, 351 (2008).
28. C. Boyer and B. Fanget, Chem. Eng. Sci. **57**, 1079 (2002).
29. D. V. Kalaga *et al.*, J. Taiwan Inst. of Chem. Eng. **40**, 602 (2009).
30. H. Toyokawa *et al.*, Nucl. Instr. and Meth. Phys. Res. A **608**, S41 (2009).
31. H. R. Weller *et al.*, Prog. in Part. and Nucl. Phys. **62**, 257 (2009).
32. H.Toyokawa, H.Ohgaki, T. Mikado, and K. Yamada, Rev. of Sci. Instrum. **73**, 3358 (2002).
33. H. Toyokawa *et al.*, Proc. Part. Acc. Conf. **713** (2003).
34. C. Sun, Characterizations and Diagnostics of Compton Light Source, PhD Thesis, Duke University (2009).
35. A. Staude, J. Goebbels, Determining the spatial resolution in computed tomography–comparison of MTF and line-pair structures, International Symposium on Digital Industrial Radiology and Computed Tomography - Tu.4.1.
36. T. Z. Regier, Development of a gamma-ray beam profile monitor for the high-intensity gamma-ray source, Thesis (2003).
37. J. W.T. Heemskerk, A.H. Westra, P.M. Linotte, C.M. Ligtvoet, W. Zbijewski, and F.J. Beekman, Phys. Med. Biol. **52(8)** N149-N162 (2007).
38. A. H. Westra *et al.*, IEEE Trans. Nucl. Sci. **56(5)** 2559-2565 (2009).